UNIVERSITY OF OKLAHOMA

GRADUATE COLLEGE

STRESS ANALYSIS OF RECENT EARTHQUAKES IN OKLAHOMA

A THESIS

SUBMITTED TO THE GRADUATE FACULTY

in partial fulfillment of the requirements for the

Degree of

MASTER OF SCIENCE

By

WEN QI
Norman, Oklahoma
2016

STRESS ANALYSIS OF RECENT EARTHQUAKES IN OKLAHOMA

A THESIS APPROVED FOR THE
CONOCOPHILLIPS SCHOOL OF GEOLOGY AND GEOPHYSICS

BY

_____
Dr. Ze'ev Reches, Chair

_____
Dr. Xiaowei Chen

_____
Dr. Brett Carpenter

Acknowledgements

First of all, I would like to express my sincere gratitude to my advisor Dr. Ze'ev Reches for his kind supporting and wise enlightenment in my three years of Master study. Without him, this thesis will never be possible. I would also like to thank my committee members Dr. Xiaowei Chen and Dr. Brett Carpenter for their valuable advising and comments in this thesis and my graduate study. Many thanks to Dr. Austin Holland for providing me the dataset and helping me throughout the thesis. I would like to thank my friends Simon, Chance, Jianjun, Zonghu, Xiaofeng, Guiyu, Jing, Da and Wiki for their support and help in my study and life. They have been so kind and helpful, and my study in University of Oklahoma has become more enjoyable because of them. Last but not least, I would like to thank my parents for their love and care throughout my whole life, for supporting me studying in United States. Without them, I could not accomplish my master thesis.

Table of Contents

List of Tables

List of Figures

Abstract

The central US, especially Oklahoma, has become a seismically active region since 2009. Knowing the current stress state of the crust in Oklahoma is essential for understanding this activity increase. My thesis focuses on stress analysis with two main objectives. First, using a stress inversion method to reconstruct the state of stress from focal-mechanisms of 562 events for the 2010 to 2015 period. The other objective is the calculation of the stress change on subsurface faults under the stress state derived from the first part.

The stress inversion method (Reches, 1987) allows calculations for stress state, discrimination between 'real' and 'auxiliary' planes of the focal-solution, and determination of the best-fit, effective friction coefficient. The determined friction coefficient is $\mu = 0.2$, and the stress state indicated a strike-slip faulting regime with partial transition to normal faulting. The direction of the minimum horizontal compression, σ_{hmin}, is 350°-360° for the entire Oklahoma region. I then evaluated the Coulomb stress on the faults with the focal-mechanism solutions by application of the in-situ stress in the Coulomb dislocation program (Toda et al., 2011). It was found that faults trending NE-SW increased their tendency for right-lateral slip, and faults trending NW-SE increased tendency for left-lateral slip. Most faults do not have reverse slip, whereas some faults have normal slip tendency. The stress change calculations are in good agreement with the stress inversion results.

Chapter 1: Introduction

Overview

The increased seismic activity in central US since 2009, and especially in Oklahoma-Kansas, was in contrast to the view of a stable tectonic region in the central part of the American plate. As a result of this activity, the seismic hazard in Oklahoma rose dramatically to become the region with the highest hazard forecast for 2016 in central and eastern US (Fig. 1A) (Peterson et al., 2016). This seismicity also raised questions about its source and mechanism, and the current general view attributes the activity rise to injection of wastewater (Ellsworth, 2013; Keranen, et al., 2013; Holland, 2013; Walsh III and Zoback, 2015).

The present analysis focuses on the crustal stresses associated with Oklahoma earthquakes by using focal-mechanisms from the 2010-2015 period. This analysis has two main objectives: (1) Determination of the current, in-situ stress state and the temporal stress changes in Oklahoma; and (2) Determination of the likelihood of fault activation by evaluating the stress change on known, subsurface faults. I used the stress-inversion method of Reches (1987, 1990) for the first objective, and the dislocation stress software (Coulomb by Toda et al., 2005, 2011) for the second objective. It is anticipated that the combination of these methods will lead to a better evaluation of Oklahoma earthquake activity.

A. B.

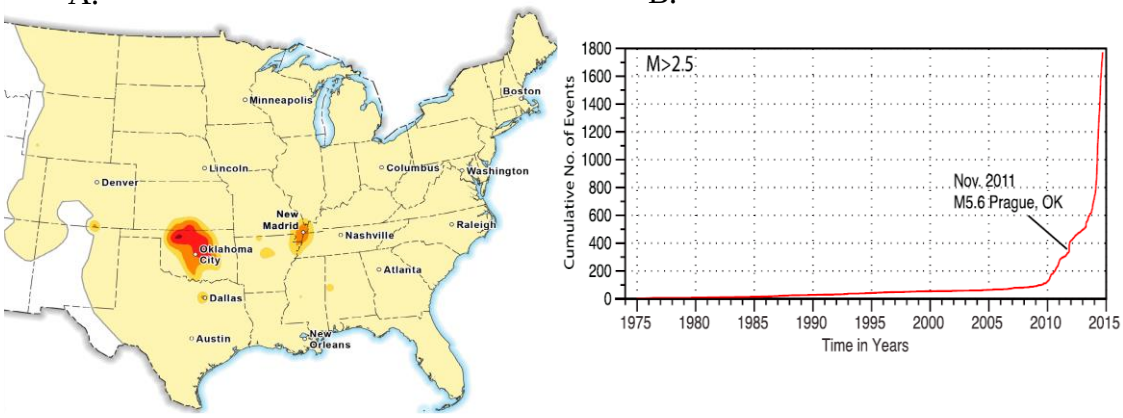

Fig. 1A: One-year earthquake hazard forecast for the central and eastern US from induced and natural earthquakes (Peterson et al., 2016). The warmer the color, the higher seismic intensity. Fig. 1B Earthquakes in Oklahoma from 1975 to December 2014, magnitude > 2.5 (McNamara, et al., 2015).

Oklahoma Geological Setting

Oklahoma is commonly divided into five major uplifts and six major basins (Fig. 2) (Johnson, 2008). The main uplifts are: Nemaha uplift in north central OK, which may extend hundreds of kilometers northward, Ozark uplift in northeastern Oklahoma, Wichita-Arbuckle uplift, which is part of the Southern Oklahoma Aulacogen, and the thrusted-folded complex of Ouachita uplift in the southeast. The north-trending fault system of the Nemaha uplift separates the very deep (> 10 km) Anadarko basin from the Cherokee platform (Northcutt and Campbell, 1998). The main mountain belts in Oklahoma are the Ouachita, Arbuckle, and Wichita systems, located in southern Oklahoma (Johnson, 2008). These belts include dense networks of faults, folds and uplifts that developed primarily during the Pennsylvanian, and exposed Precambrian-Cambrian igneous rocks and thick sequences of Paleozoic sedimentary sequences.

Fig. 2. Oklahoma geological provinces (Johnson, 2008).

Oklahoma Earthquakes

The New Madrid earthquakes (M = 7.6-8.0) in 1811and 1812 are the largest and earliest historical earthquakes in the central US, close enough to be felt in Oklahoma (Luza, 2008). The earliest earthquake epicenter documented in Oklahoma was in October 22, 1882; the location was poor but MM VIII intensity near Fort Gibson, Indian Territory (Stover et al, 1983). The earliest documented locatable earthquake occurred near Jefferson in Grant County on December 2, 1897 (Storver et al., 1983). Until the recent activity, the 1952 M=5.5 El-Reno earthquake was the largest known Oklahoma earthquake. It was felt in an area of 140,000 square miles, and produced MM VII-IX intensity effects near the epicenter (Luza, 2008).

Prior to 1976, most Oklahoma earthquakes occurred in Canadian County (Luza, 2008). The majority of them were located in the vicinity of El Reno, where a series of earthquakes occurred since 1908. Other main areas of seismicity are in Love, Carter and Jefferson counties, with the first reported earthquake in these counties during 1974

(Luza, 2008). The Arkoma basin, in southeast Oklahoma, is another area of active seismicity (Luza, 2008).

Oklahoma, considered a tectonically stable area away from a tectonic boundary, faced a rise of seismic activity starting in 2009 (Fig. 1B). This activity included several large earthquakes, e.g., Prague 2011 M=5.6 event (Keranen, et al., 2013). The increase of both seismicity and magnitude in Oklahoma indicates that the annual rate of earthquakes of magnitude $M \geq 3$ exceed the equivalent in California since 2014 (McGarr, et al., 2015).

The increase in recorded seismic activity of Oklahoma is due, partly, to improvement in seismic detection, but the increase of M >3.0 earthquakes in real. The lower magnitude events exist, but are not detectable at this time. The Oklahoma Geological Survey placed new seismometers and added new seismic monitoring stations. Thanks to the increasing number of stations, more earthquakes, including small magnitude earthquakes (M<3) were detected. Typically, Oklahoma earthquakes have magnitude ranging from 1.8 – 2.5, with shallow focal depths less than 4.5 km (Luza, 2008). In 2009 and 2010, the NSF EarthScope U.S. Array program developed seismic monitoring stations at 70-km spacing across Oklahoma (USArray website). Fig. 1B shows the cumulative numbers of earthquake events in Oklahoma, starting from 1975 to December 2014. The Prague earthquake, with magnitude 5.6 in November 2011, has been pointed out in the plot (McNamara, et al., 2015).

Chapter 2: Methods and Data of Present Study

Stress-Inversion Analysis

General

Stress-inversion is a numeric method to determine the state of stress that can cause slip along a group of faults (Angelier, 1984). Bott (1959) made the widely accepted assumption that slip along a fault occurs parallel to the direction of maximum resolved shear stress, and essentially all stress-inversion methods are based on this assumption.

Angelier (1984) utilized the direction and slip sense on individual faults to calculate the reduced stress tensor with the orientations of the stress axes. This method allows the use of data on new faults created by tectonic loading and/or reactivated old discontinuities by a new stress field. This work also demonstrated the use of earthquake focal-mechanisms and analysis of heterogeneous data sets to distinguish successive fault events (Angelier, 1984).

Gephart and Forsyth (1984) assumed that a uniform stress state in a source region controlled the orientations and slip directions of earthquake focal-mechanisms, and they used this assumption to determine a best fit for the principal stress axes. They also allowed the failure to occur on preexisting zones of weakness of any orientation. Their method finds the solution that requires the smallest total rotation of all the fault planes that is needed to match the difference between the observed and predicted slip directions (Gephart and Forsyth, 1984).

Michael (1984) used slickenside data of the stress field to find the single uniform stress tensor that is most likely to cause faulting events. He assumed that the

magnitude of the tangential traction on the various fault planes was similar at the time of rupture (Michael, 1984). The direction of the maximum tangential traction on the plane tends to be parallel to the slip direction.

The above models of Angelier, Gephart and Michael, can be used for field observations and focal mechanisms for stress inversion. These models use the average difference between the calculated shear stress direction and the actual slip axis on faults as estimators of the solution accuracy.

The Present Stress-Inversion Method

Assumptions

I used a stress-inversion program called "Stress" that was developed by Reches (1987, 1990). It is available as part of the SoftStructure package (http://earthquakes.ou.edu/reches/soft.html). This method is based on three assumptions:

1. Slip along a fault occurs parallel to the direction of the maximum resolved shear stress on this fault (similar to Bott, 1959).

2. The stress state that maintains the slip obeys the Coulomb-Anderson Failure Criteria:

$$|\tau| \geq C + \mu\, \sigma_n,$$

where C is the fault cohesion, and μ is its friction coefficient, τ and σ_n are the shear and normal stresses. This assumption of Coulomb friction law is unique to this method.

3. The slip events along the group of faults occurred under relatively uniform conditions:

   a. The faults were activated under the same stress state.

   b. The friction of the faults may be represented by the mean value of the group.

Advantages

The Stress program calculates a stress tensor that can cause slip frictional faults, whereas previous inversion methods implicitly assumed that the faults are friction-less (Reches, 1987). The slip misfit criterion was used by Angelier (1984), Gephart and Forsyth (1984), and Michael (1984) without considering friction coefficient, and Reches (1987) showed that such stress-inversion implies that $\mu = 0$. Reches (1987) also demonstrated that the calculated stress solutions vary with different friction coefficients.

The solution quality is evaluated with two misfit angles (Angelier, 1984; Reches, 1987). The first is 'slip misfit' (SM) angle, which is the average difference between the calculated axis of maximum shear stress for each fault, and the actual (measured) slip axis on the same fault. The second is the 'principal axes misfit' (PAM), which is the average difference between the calculated principal axes directions for whole fault set and the ideal, principal axes directions for each fault. The principal axes misfit criteria allows to distinguish between the two nodal planes of an earthquake focal solution (Reches, 1990), and to estimate the mean friction coefficient.

Focal-Mechanism Solution of Earthquakes

The present stress-inversion analysis was conducted on 562 focal-mechanism solutions of Oklahoma earthquakes. These focal-mechanism solutions (FMS), for the period January 14, 2010 to February 14, 2015, were determined by Dr. Austin Holland, Oklahoma Geological Survey, who kindly provided his results for the present analysis. This dataset has 562 FMS including information of earthquakes origin time, location, magnitude, epicenter depth, strike, dip, rake, P-trend, P-plunge, T-trend and T-plunge.

Focal-mechanism solution refers to fault plane and the slip direction during an earthquake (Shearer, 1999). These solutions are determined from data of multiple seismic stations to derive the fault planes that are associated with the earthquake (Sipkin, 1982, 1986, 1994). The focal-mechanisms display a “beach ball”, of two equivalent planes with their corresponding slip axes (Fig. 3). The “beach ball” is the stereographic projection of these two planes, one is considered the fault plane and the second the auxiliary plane that is perpendicular to the fault plane (Fig. 3). It is not possible to distinguish between the two for small earthquakes. Both fault plane and axillary plane are considered as the ‘nodal planes’. The shaded area is the section of compression, and the bright area is the extension section. Traditionally, focal-mechanisms are computed by finding the best-fit direction of the up-or-down motion of the first arrival of P-wave (Shearer, 1999).

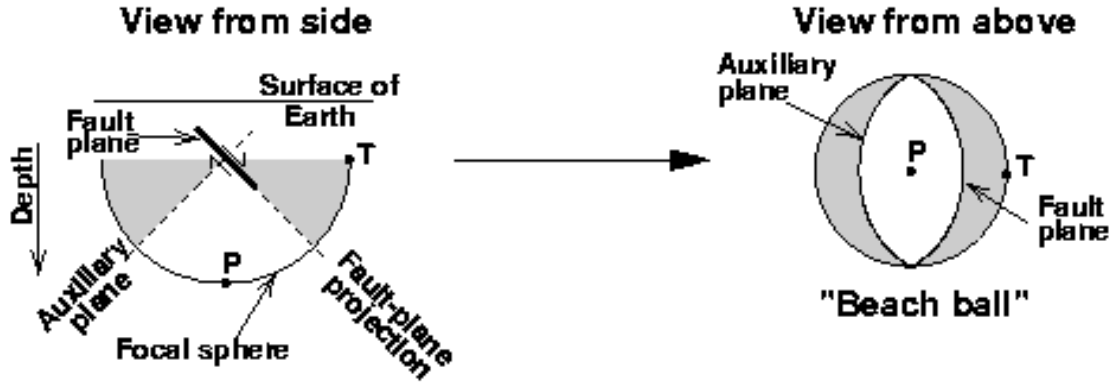

Fig. 3. Schematic illustration of focal sphere view from side and beach ball view from above (USGS, 1996). P: P-axis, the “Pressure” axis or compressional axis. T: T-axis, the “Tension” axis.

Fig. 4 shows three examples of focal-mechanisms. The left diagram indicates a strike-slip fault; the middle is a normal fault, and the third one represents a thrust fault or a reverse fault. In this “double couple” configuration, the auxiliary plane does not

have a geological meaning, but for small earthquakes without surface rupture or additional information, the focal-mechanisms is insufficient to indicate the actual fault plane. Later, the present stress-inversion provides a tool to solve this double-couple difficulty.

Fig. 4. Focal-mechanism "beach ball" diagrams. Example of strike-slip, normal and reverse fault (Cronin, 2010).

Dislocation Stress Calculations: Coulomb3.3 Software

I used the Coulomb3.3 software (Toda et al., 2005, 2011) to calculate stress change on prospective faults in Oklahoma. Coulomb3.3 calculates the static stresses, strains, and displacement generated by slip on faults or expansion dikes. The slipping faults are simulated as rectangular, planar dislocations embedded in a linear, elastic half-space. The slip along a dislocation changes the stress-field in the space around it (Toda, et al., 2011), and modifies the stress state on other faults that did not slip.

The program calculated the changes of the stress components on receiver faults in an elastic half space. These components are related to the Coulomb failure criterion, which is the widely used criterion for fault slip (Byerlee, 1978).

The original Coulomb law of failure is:

$$\tau = C + \mu \sigma_n,$$

where τ is shear stress, μ is friction coefficient, C is cohesion, and σ_n is the normal stress. Assuming that C = 0 for preexisting faults,

$$\tau = \mu \sigma_n,$$

which is Byerlee's Law (Byerlee, 1978). It indicates that the critical shear stress that can cause the slip of preexisting faults is equal to the coefficient of friction on the fault times the normal stress on the fault plane.

The component in Coulomb program calculations are defined by the changes, Δ, due to the slipping fault. Rearranging Byerlee's Law, we get,

$$\Delta CFF = \Delta\sigma_f = \Delta\tau_s + \mu'\Delta\sigma_n,$$

where ΔCFF is the 'Coulomb Failure Function' that equals $\Delta\sigma_f$, the stress change on the potential, receiver fault by slip along source fault(s), $\Delta\tau_s$ is shear stress change, and $\Delta\sigma_n$ is normal stress change. μ' here is the effective friction coefficient of a fault. A receiver fault may fail if ΔCFF increases due to slip on the source fault(s). A stress shadow for one receiver may be a stress trigger zone for another receiver fault.

The program can calculate stress changes of four types of receiver faults: (1) "specified" receiver faults, meaning all faults that have a uniform receiver fault geometry, (2) faults optimally oriented for failure, (3) receiver faults that are built in the input file, and (4) focal-mechanism files, in which there are always two nodal planes. The optimal orientations are a function of the regional or tectonic stress and the source faults. The friction coefficient is a requirement of receiver faults during calculations. Coulomb3.3 provides diverse calculations options like stress in cross-section and at different calculation depth (Toda, et al., 2011).

With Coulomb3.3, I calculated the stress change on faults in Oklahoma under calculated current stress state. This program is available at http://usgsprojects.org/coulomb/

Data Analysis of Oklahoma Faults and Earthquakes

Oklahoma Faults

The Oklahoma faults dataset includes the digital map of faults in Oklahoma that was compiled by the Oklahoma Geological Survey (Darold and Holland, 2015). This set includes the coordinates of starting and ending points of segments of surface and subsurface faults. It was extracted from Oklahoma geologic maps and subsurface data. Fig. 5 shows the Oklahoma fault segment traces plots with 23,665 km of cumulative length. In my thesis, I will use the locations and orientations of the fault segment traces, and compare them with my focal-mechanism data.

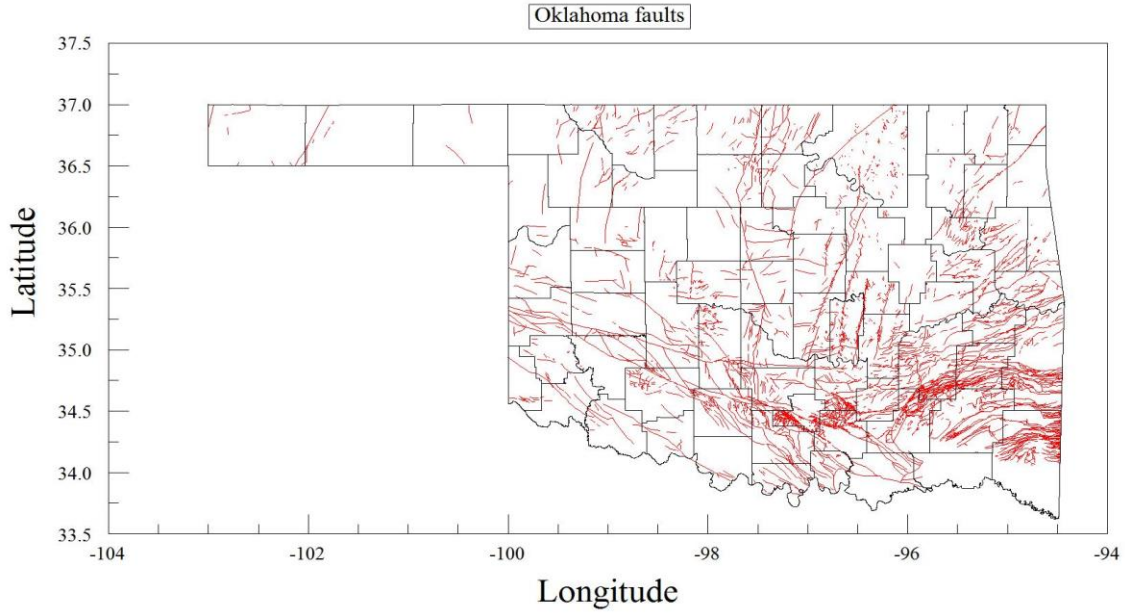

Fig. 5. Oklahoma fault segment trace map (after Darold and Holland, 2015).

Chapter 3 Stress-Inversion Analysis

Time History of the Recent Oklahoma Earthquakes

In the first step of the analysis, I clustered the FMS data into four time groups. Fig. 6 displays the frequency of the FMS (number of events per 10-day intervals) in the database (01/14/2010 to 02/14/2015). For stress evolution calculations, I divided the solutions into four time groups (Fig. 6, Table. 1). Group "OK-1" has relatively low FMS frequency, less than 5 per ten days. The earthquake spike of OK-2 with nearly 35 per ten days is associated with the many aftershocks of the Prague M5.6 2011 earthquake. OK-3 follows the OK-2 spike with frequency similar to OK-1 group. The last group, OK-4, has a high and variable frequency, ranging 5-25. It should be noted that Fig. 6 reflects only the time frequency the 562 available FMS and is does not necessarily indicate the time frequency of the seismic activity. I will use these time groups to determine stress evolution. The locations of the four group events (Fig. 7) indicates a likely migration trend of the earthquakes from south-southeast to north-northwest. The A, B, and C zones in Fig. 7 are the same fault map zone division in later discussion (Fig. 14). Note that nearly all FMS are in zone B.

Table. 1: Four seismicity groups division.

Subgroup#	Start—End Date	Total Days	Numbers of Events
OK-1	01/14/2010—10/28/2011	652	103
OK-2	10/28/2011—02/07/2012	102	51
OK-3	02/07/2012—07/01/2013	510	39
OK-4	07/01/2013—02/14/2015	593	369

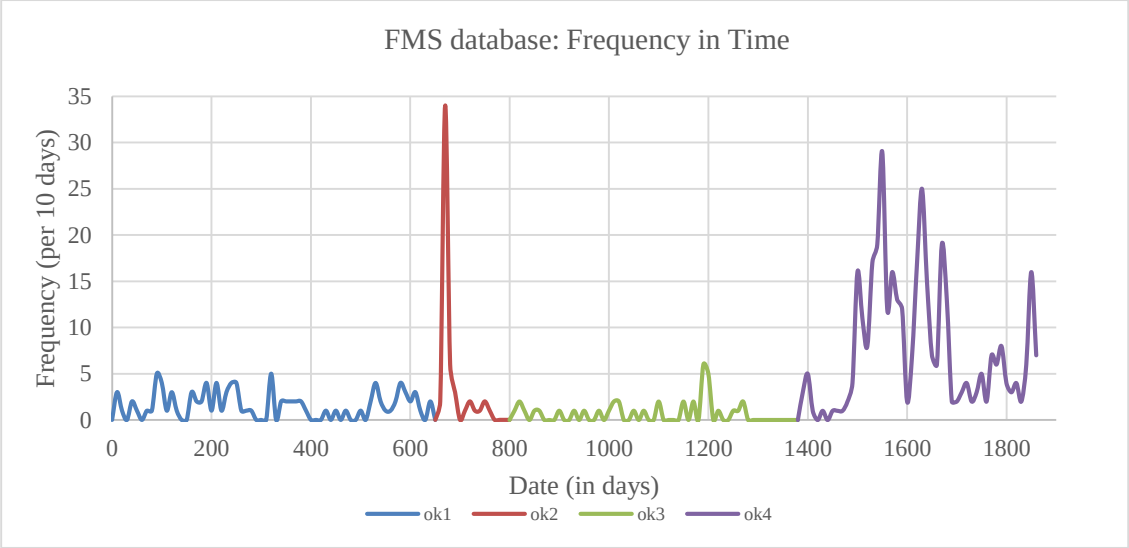

Fig. 6. Time frequency of the focal-mechanism dataset. This dataset is divided into four groups based on their events frequency. OK-1 low frequency; OK-2 spike for aftershocks of the Prague 2011 earthquake; OK-3 low frequency; OK-4 variable frequency.

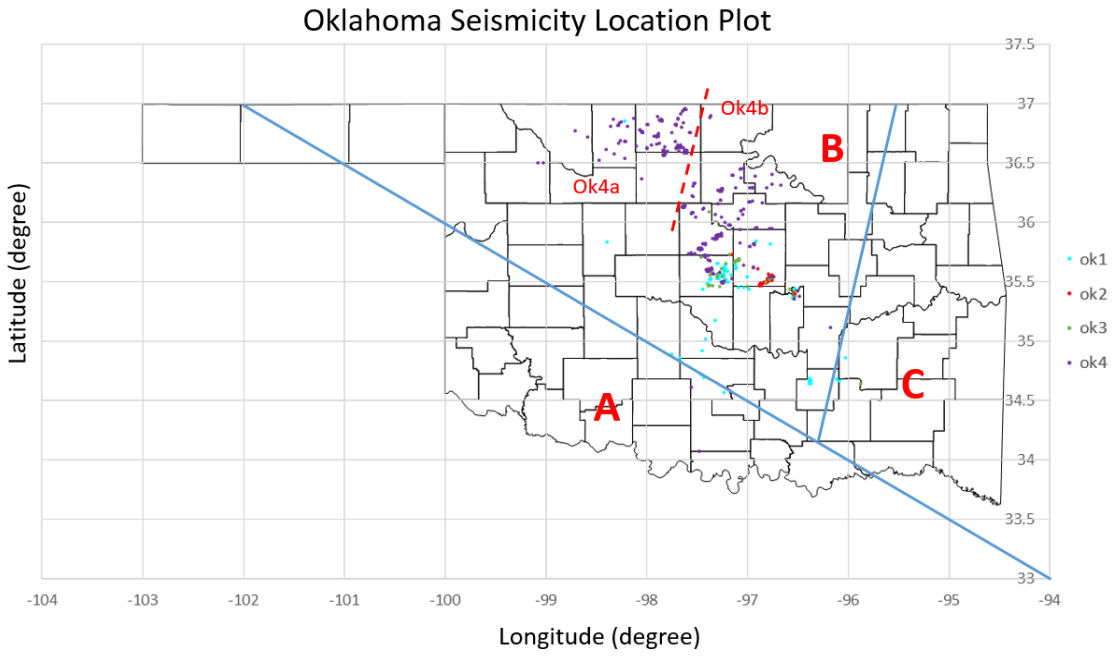

Fig. 7. Oklahoma FMS location plot, groups are same as the clustered group in Fig. 6. Each dot representing one earthquake event from the FMS dataset.

Different color stands for different groups. Ok1: blue, Ok2: red, Ok3: green, Ok4: purple. Red dashed line separate the Ok4 into two subgroups, and the stress state of the subgroups Ok4a and Ok4b will be discussed in section Stress State Fig. 12. A, B, and C are fault map divisions based on Oklahoma structural geology map, and will be discussed in Figs. 14, 15. Oklahoma county boundary are after Oklahoma Geological Survey, 2016, County data.

Stress-Inversion Calculations

Friction Analysis

Every FMS is a 'double-couple' with one plane of the 'real' fault and the second is the auxiliary plane. The first step in the stress-inversion with the Stress program was to select the more likely 'real' fault by using the 'principal angle misfit' (PAM) (Reches, 1990). This procedure also indicates the most suitable friction coefficient for the analyzed faults (Reches et al., 1992).

Running the Stress program requires input for a friction coefficient range and step, mean cohesion of the fault, pore pressure, and input file. The program calculates the results of the entire fault set including: stress tensor; principal stress σ_1, σ_2, and σ_3; stress ratio; friction deviation; misfit angles (mean angle between observed and calculated slip axis and mean angle between general and ideal principal stress axes). These results are calculated for one friction coefficient, and the program progresses to next friction coefficient. By going through different friction coefficients, the calculated misfit angles can be used to evaluate the best-fit friction coefficient.

I processed the four groups for the complete range of friction coefficients with two different criterions. Slip misfit and Principal Axes Misfit (PAM) versus friction

coefficient are plotted in Fig. 8 and Fig. 9, respectively. PAM varies non-monotonically with friction coefficient, whereas Slip Misfit (SM) always increases with higher friction coefficient, thus the lowest SM is always at μ =0 (Fig. 8). Fig. 9 shows that PAM decreases from μ = 0.01 to μ = 0.2, and increases for μ > 0.2. Thus, I used μ = 0.2 for all groups in the following stress inversion.

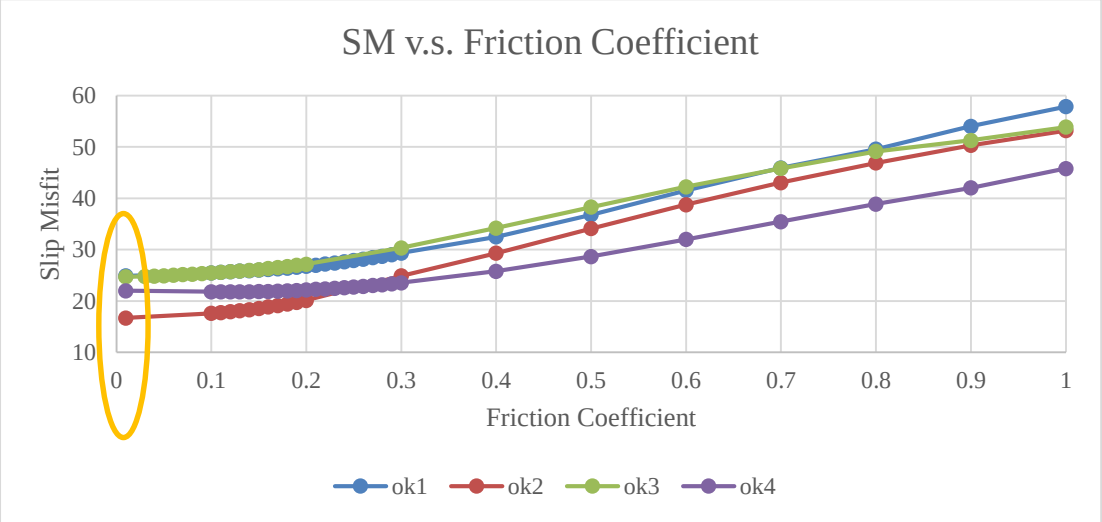

Fig. 8. Slip misfit value versus friction coefficient for the four groups (legend).

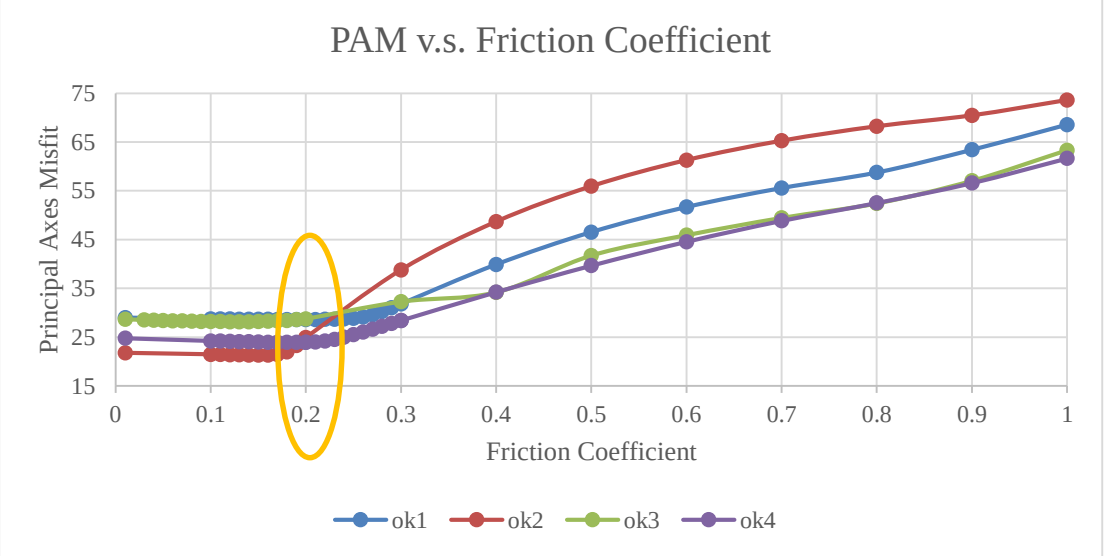

Fig. 9. Principal axes misfit versus friction coefficient for the four groups (legend). The lowest PAM is for μ =0.2.

Based on the second assumption of Reches (1987) stress inversion method discussed earlier,

$$|\tau| \geq C + \mu\, \sigma_n,$$

I also test on the principal axes misfit change with respect to cohesion when friction coefficient is fixed. I chose a typical rock friction coefficient of □□□□0.6 for this analysis. The result is plotted in Fig. 10 for the four different groups. The cohesion values are percentage of vertical stress, so the full range of cohesion here is 0-1. Between 0 to 0.2, the step of cohesion (C) is 0.01, which is 1% of the vertical stress.

Fig. 10 shows that for C < 0.1 (10% of vertical stress), all four groups display a stable PAM, and for C > 0.1, the PAM starts to rise. This result suggests that for the stress inversion of the current dataset, cohesion of less than10% of vertical stress results in the best fit.

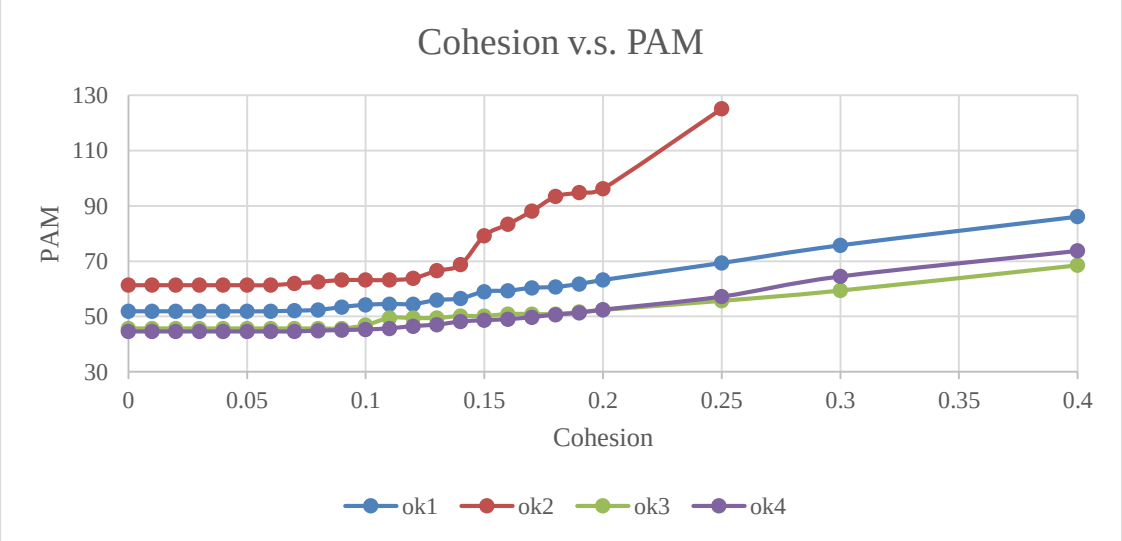

Fig. 10. Principal axes misfit versus cohesion for the four groups (legend), μ = 0.6.

In the Stress program, at selected friction coefficients, options for further examinations include: examine each fault results, display misfit angles and deletion of faults, automatic deletion of focal-mechanisms, and saving the calculated stress tensor

for use in other programs. I chose to separately examine each fault's results. Then each focal-mechanism event is evaluated in pairs starting with fault#1 and fault#2. I compared PAM and SM for the two nodal planes of each event in FMS, and selected the plane with smaller value of PAM as the 'real' fault plane that slips; the other one will be deleted. After selecting the whole input file, the selected faults were saved for the inversion.

Stress State

Stress State by Groups

The Stress program calculates the best-fit stress tensor for slip along all faults in the group for the given friction coefficient. The stress tensor results include the orientations of principal stress axes and magnitude of the principal stresses, relative to the vertical stress. The confidence range of the axes orientations is calculated by the 'bootstrap method' after Michael (1987), in which 500 iterative solutions are determined for the same fault set.

The orientations of the principal stresses of the four groups (crosses in Fig. 11) are plotted with the confidence range as a 'cloud' of iterative solutions (open small circles in Fig. 11). Mean axes with radius of confidence are listed in Table. 2 for the four groups separately and the 562 events. Table. 3 has information of principal stress magnitudes for all groups. Stresses are given by the units of the vertical stress, overburden load, and are normalized by its magnitude. Negative value means compressive. And the vertical stress here is -100.

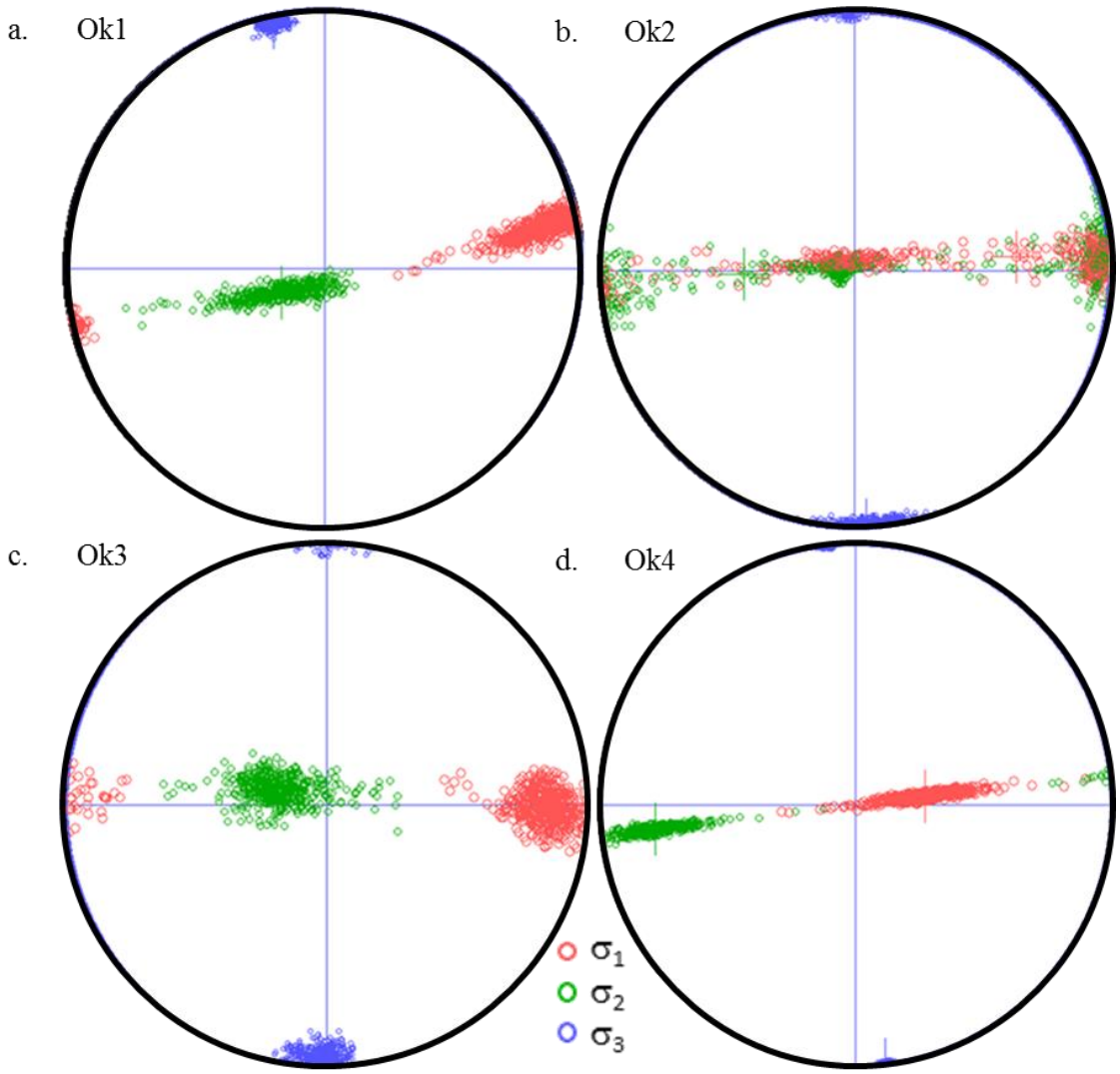

Fig. 11. Orientations of the calculated principal stress axes, σ_1, σ_2, and σ_3 are marked as red, green and blue circles, respectively. Mean axes are in crosses, and the 500 iterative solutions are in small circles of the corresponding color.

Table. 2: Mean axes (plunge/trend ±range of confidence) of the three principal stresses for each group and whole dataset shown in Fig. 11, 12 and 13.

Group#	μ	Criterion	σ_1	σ_2	σ_3
Ok1	0.2	PAM	$14°/79° \pm 19°$	$74°/241° \pm 19°$	$4°/348° \pm 4°$
Ok2	0.2	PAM	$36°/85° \pm 76°$	$53°/268° \pm 76°$	$2°/177° \pm 8°$
Ok3	0.2	PAM	$15°/90° \pm 18°$	$74°/287° \pm 18°$	$4°/181° \pm 9°$
Ok4	0.2	PAM	$67°/82° \pm 18°$	$22°/263° \pm 18°$	$0°/173° \pm 1°$
Ok4a	0.2	PAM	$56°/79° \pm 53°$	$33°/263° \pm 53°$	$1°/172° \pm 3°$
Ok4b	0.2	PAM	$26°/84° \pm 44°$	$63°/263° \pm 44°$	$0°/354° \pm 1°$
All	0.2	PAM	$38°/90° \pm 29°$	$51°/262° \pm 29°$	$0°/352° \pm 2°$
All	0.01	SM	$3°/82° \pm 4°$	$86°/282° \pm 4°$	$1°/172° \pm 2°$

Table. 3. Magnitude of principal stresses for each group (values are relative to vertical stress, which is -100).

Group#	μ	Selection Criterion	Number of Events	Average Misfit Angle		Magnitude of Stresses		
				PAM	SM	σ_1	σ_2	σ_3
Ok1	0.2	PAM	103	30.57	30.82	-109	-100	-70
Ok2	0.2	PAM	51	17.16	17.31	-101	-100	-67
Ok3	0.2	PAM	39	28.22	25.22	-112	-99	-72
Ok4	0.2	PAM	369	26.57	22.12	-100	-98	-63
Ok4a	0.2	PAM	119	25.46	21.27	-100	-97	-63
Ok4b	0.2	PAM	250	25.89	24.63	-100	-99	-64
All	0.2	PAM	562	26.30	24.28	-102	-99	-65
All	0.01	SM	562	25.14	22.33	-104	-100	-67

Group Ok4

Observing Fig. 7, the locations of FMS, I found that Ok4 could be subdivided into to Ok4a and Ok4b. The red dashed line in Fig. 7 crudely represents the Nemaha fault, which is a regional structure that separates these subgroups. Ok4a is those events occurred on the west of Nemaha fault, and the Ok4b is to the east of the Nemaha fault. Stress inversion of these two groups are processed and plotted in Fig. 12 below. The mean axes and magnitude of three principal stress are in Table. 2 and Table. 3.

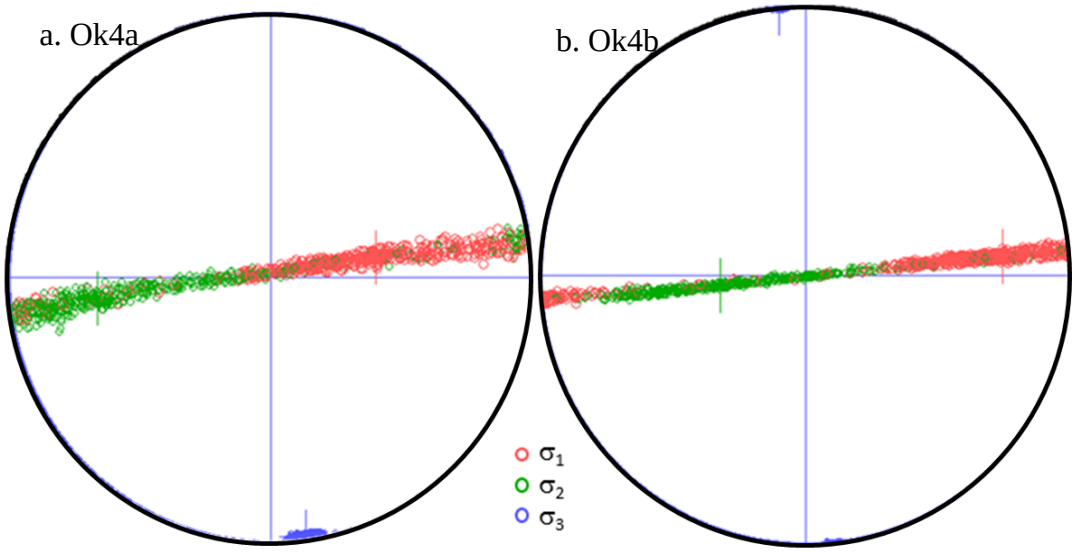

Fig. 12. Orientations of the calculated principal stress axes, σ_1, σ_2, and σ_3 of Ok4a and Ok4b, respectively. Mean axes are in crosses, and the 500 iterative solutions are in small circles of the corresponding color.

The stress state of Ok4a and Ok4b in Fig. 12 indicates that:

a. Both Ok4a and Ok4b show an oblique strike-slip fault system.
b. The western area of Nemaha fault (Ok4a) has stronger component of normal slip.

c. The eastern regime of Nemaha fault (Ok4b) has smaller component of normal slip.

Nemaha fault separated the two groups Ok4a and Ok4b naturally. The stress state in two sides of Nemaha fault are slightly different. This may related to geology of Nemaha fault.

Entire dataset

Fig. 13 a, b shows the result of the stress-inversion for the whole dataset under SM and PAM correspondingly. The inversion results entire group of 562 FMS were calculated with μ = 0 for the SM (Fig. 13a) and μ = 0.2 for PAM (Fig. 13b). These solutions reveal a wide spread pattern of σ and σ_2, and a very focused σ_3 for both cases, and the SM solution (Fig. 13a) is for pure strike-slip conditions, whereas the PAM solution (Fig. 13b) indicates a transition of strike-slip and normal faulting conditions.

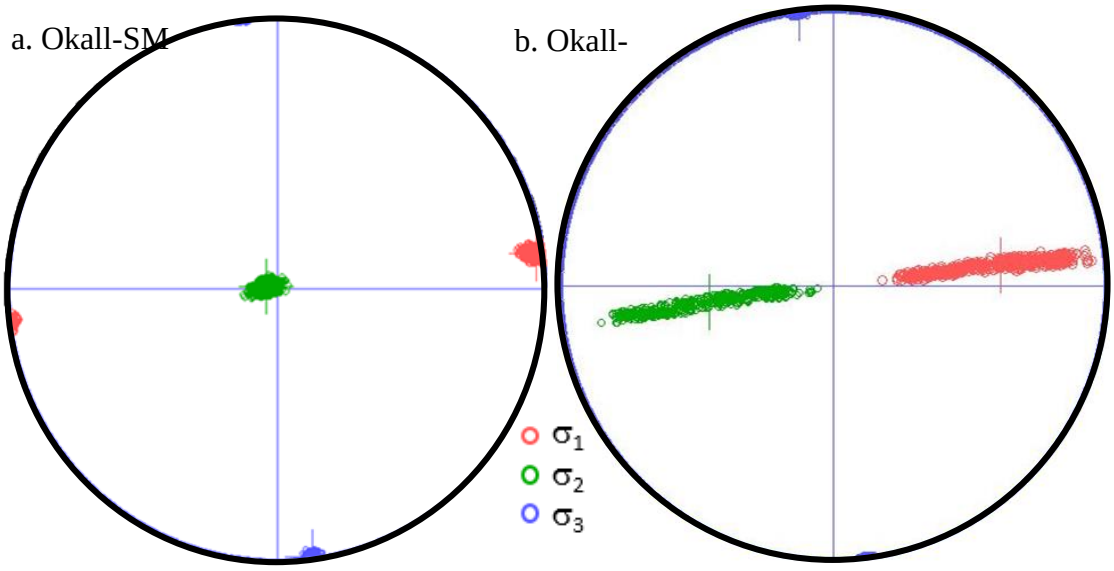

Fig. 13. Stress-inversion 500 solution of random selection for all 562 focal-mechanisms picked with: a. lower SM under μ = 0.01; b. lower PAM under μ = 0.2.

Summary: Stress State Description

In general, all the inversion solutions display a consistant pattern for the five year period of observation (Fig. 6), and the large area of earthquakes (Fig. 7). The calculated stress state can be summerized by the following features:

a. The Principal Axes Misfit (PAM) results suggest a best-fit friction coefficient for the whole dataset is 0.2.

b. Consitant σ_3 directions throughout all groups with values of 0°/352° ±2°: narrow range of confidence, and 352° - 180° = 172°, which indicates that σ_3 in all four groups are nearly the same.

Switching between normal faulting (Ok3) and strike-slip faulting (Ok2), or mixed normal faulting and strike-slip faulting (Ok1 and Ok4).

Relations between Oklahoma Faults and Recent Earthquakes

Oklahoma Fault Systems

In this section, I compare the in-situ stresses calculated from the FMS (Fig. 13) to the fault pattern of Oklahoma as compiled by Darold and Holland (2015) (Fig. 5 and text). For sake of comparison, the fault map was divided into three zones based on different geological provinces in Oklahoma and the earthquake distribution. Zone A includes Wichita frontal fault zones, Wichita uplift, Hollis basin, Waurika-Muenster uplift, Marietta basin, Ardmore basin and Arbuckle mountains (Northcutt and Campbell, 1995). Zone B contains Arbuckle uplift, Anadarko basin and Cherokee Platform (Northcutt and Campbell, 1995). Zone C has the region of Ozark Uplift, Arkoma basin and Ouachita mountain uplift (Northcutt and Campbell, 1995). The

23,665 km of cumulative fault segments (above) were divided into the A, B, and C zones (Fig. 14) and their strike orientations are plotted in Fig. 15.

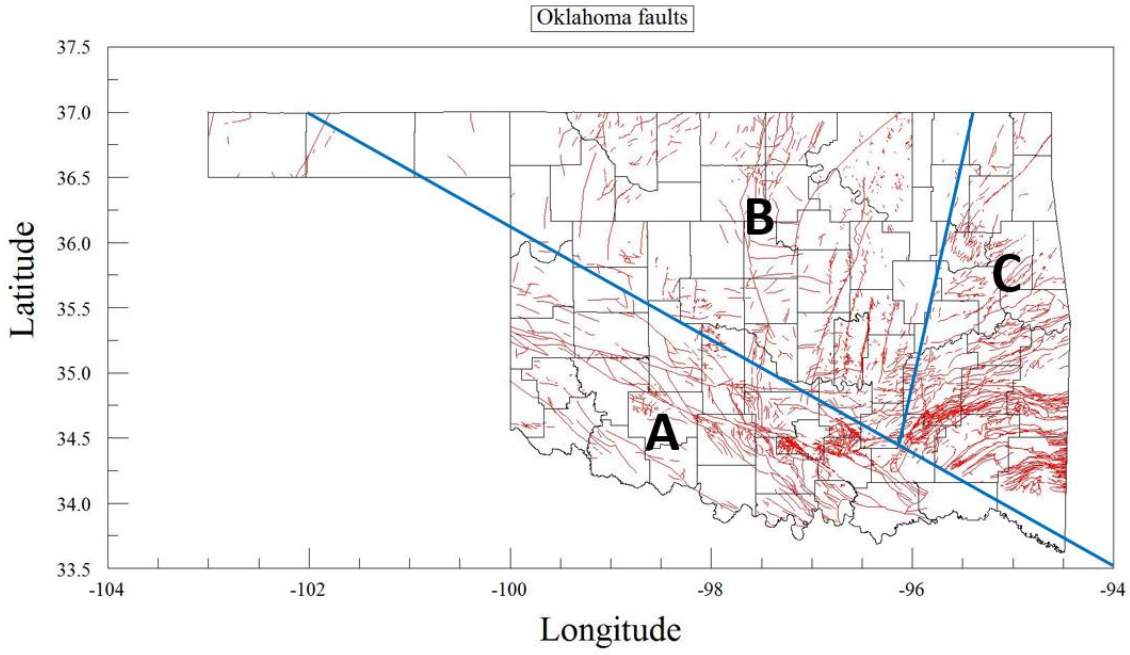

Fig. 14. Fault map in Oklahoma. Solid, blue line separate Oklahoma into three tectonic zones as discussed in the text. Strike distribution of the fault segments in zones A, B, and C is plotted via rose diagrams in Fig. 15.

Table. 4. Total length and orientations of faults in Zone A, B, and C.

Tectonic zones	Numbers of fault segments	cumulative length (km)	Dominant trends
A	10,087	9443.2	120°
B	4,033	4926.9	20°, 92°, 156°
C	12,193	9295.6	65°

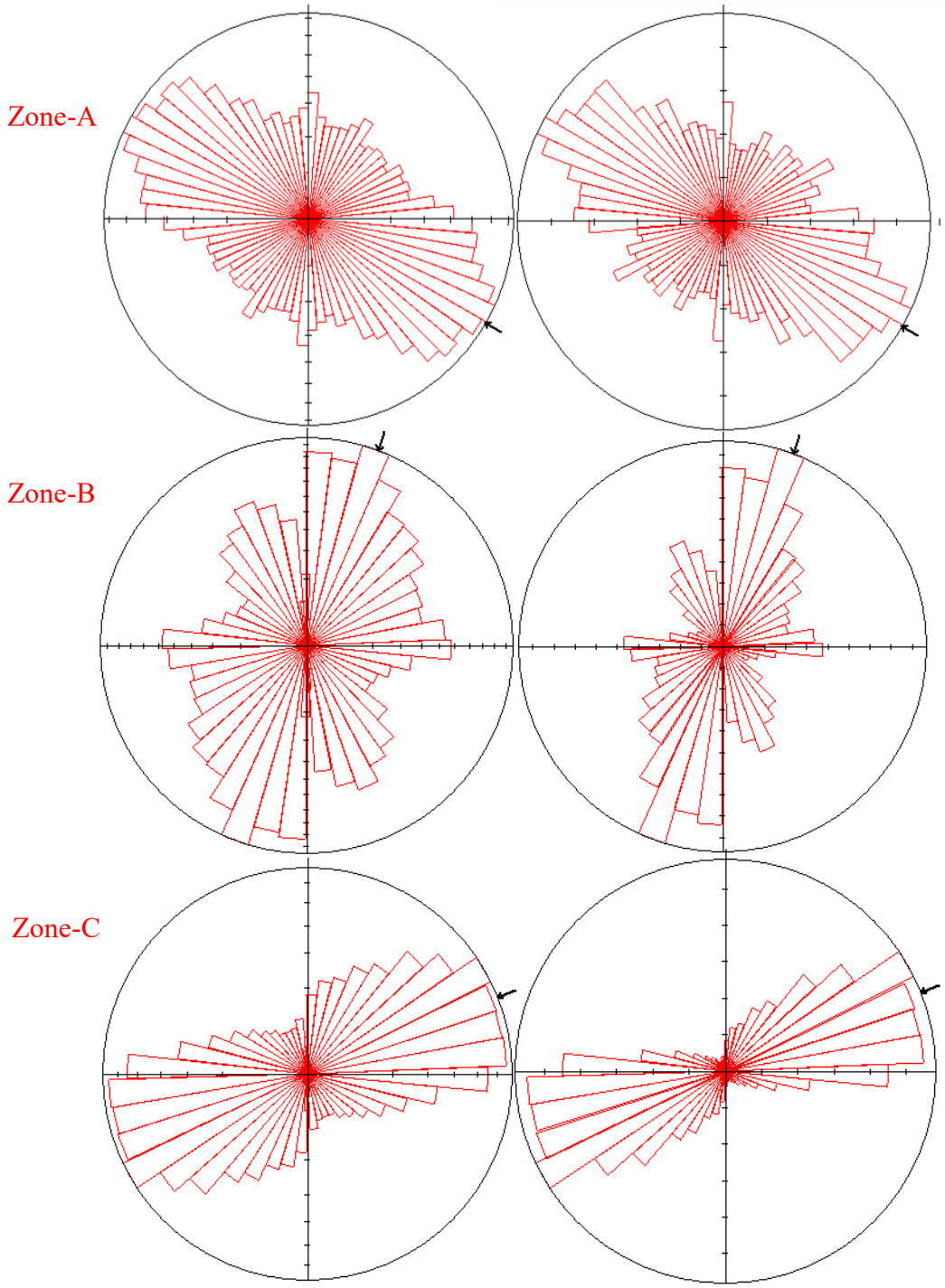

Fig. 15. Fault strikes in Oklahoma according to zones A, B and C, left column area weighted, and right column are non-area weighted. The rose diagrams are plotted with sector angle of 8º and they are scaled by their length and azimuth; plotted with GeOrient.

Comparison of Oklahoma Faults Trends and the Focal-Mechanisms

All focal-mechanism events occurred in zone B. The optimum fault strike selected based on principal axes misfit angle has a rose diagram as Fig. 16 showed, 8-degree sector and length-weighted plot.

Fig. 16 a, b, c. Comparison of fault strike rose diagram plot of all focal-mechanisms with the historical fault traces in the three zones overlaid. All fault orientations plot in area weighted, length-azimuth rose diagram, sector size is 8°. In location map Fig. 7, nearly all FMS are located in Zone B. However, Fig. 16 shows that the FMS strikes share some similarities with fault orientations in Zone A instead of Zone B.

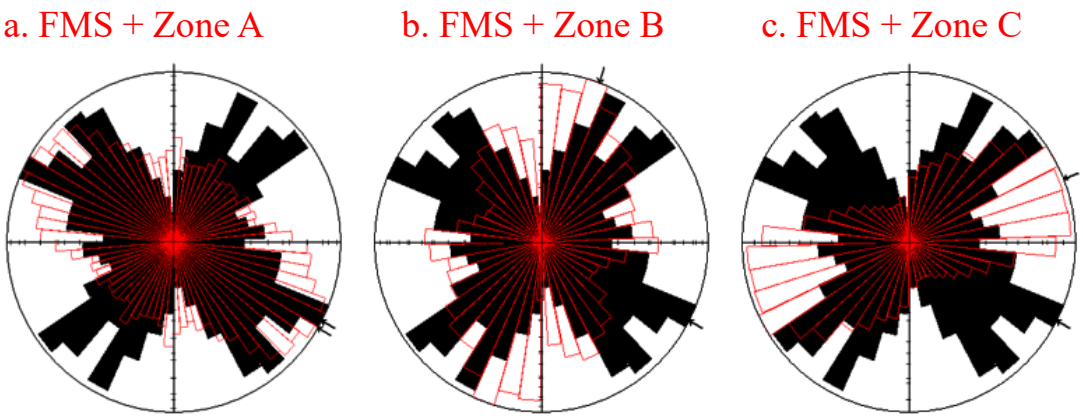

Fig. 16. Fault strike rose diagram of FMS overlaid by different fault zones (length related, area weighted, 8-degree sector): a. FMS and Zone A, b. FMS and Zone B, c. FMS and Zone C. FMS plotted here includes total dataset, and is selected under $\mu = 0.2$ based on principal axes misfit angle.

Chapter 4 Stress Analysis: Slip Potential on Oklahoma Faults

Coulomb Model Setting Up

Assumptions and Fault Conversion

The Oklahoma earthquakes are further investigated with Coulomb3.3 software (see methods), and I focus on stress changes on known faults in Oklahoma by the stress state calculated above with the stress-inversion (Fig. 13).

In the first step, I adopted the FMS that was used for the stress-inversion to fit the Coulomb program. The focal mechanisms includes the following information: Strike, α, Dip, θ, Latitude and longitude of the epicenter, x, y, Earthquake Magnitude, M, Depth of the epicenter, D. These values are also required for Coulomb3.3 input file. Plus, Coulomb3.3 requires rupture length, fault segment starting point (X-start, Y-start), fault segment finish point (X-end, Y-end), fault plane top depth h-top, and fault plane bottom depth h-bottom. For the fault sizes, I used the empirical equation from Wells and Coppersmith (1994), that correlates fault rupture area to earthquake magnitude,

$$M = 4.07 + 0.98 * log(RA) \cdots\cdots\cdots 1$$

where M is the earthquake moment magnitude, RA is the rupture area (Fig. 17).

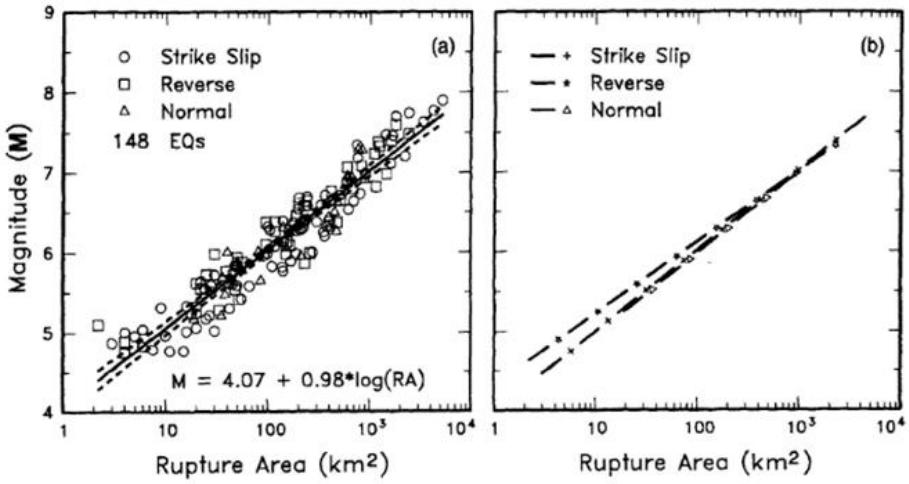

Fig. 17: (a) Regression of rupture area on magnitude (M). Regression line shown for all-slip-type relationships. Short dashed line indicates 95% confidence interval. (b) Regression lines for strike-slip, reverse, and normal-slip relationships (Wells and Coppersmith, 1994).

Thus, each focal-mechanism event is converted to a fault plane in Coulomb. A schematic illustration of the fault length calculation is shown in Fig. 18. Yellow star stands for the hypocenter, and the blue arrow indicates the fault plane strike direction. This figure is a fault plane view and the rupture length is represented by "L".

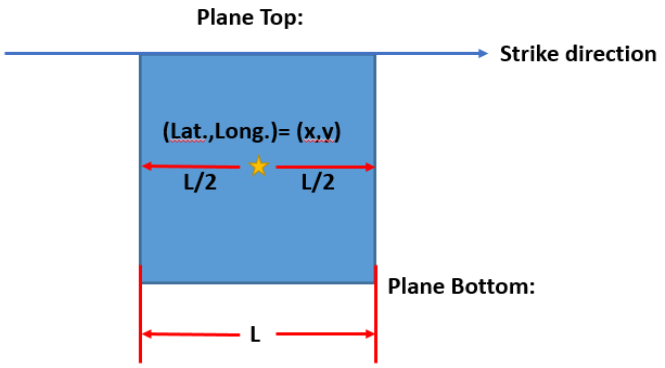

Fig. 18: Schematic illustration of assumed fault plane rupture area and rupture length calculations.

Equation #1 is used to calculate the rupture area, A, and by assuming that the faults have a square rupture area, the rupture length L is

$$L = \sqrt[2]{A} \quad \cdots\cdots\cdots\cdots\cdots\cdots\cdots\cdots\cdots\cdots 2$$

In the cross-section view, the fault plane is at the hypocenter depth D (Fig. 19). The Coulomb3.3 requires fault to have at least 1° dip, which means for horizontal fault the dip is needed to be set 1° for calculation convenience.

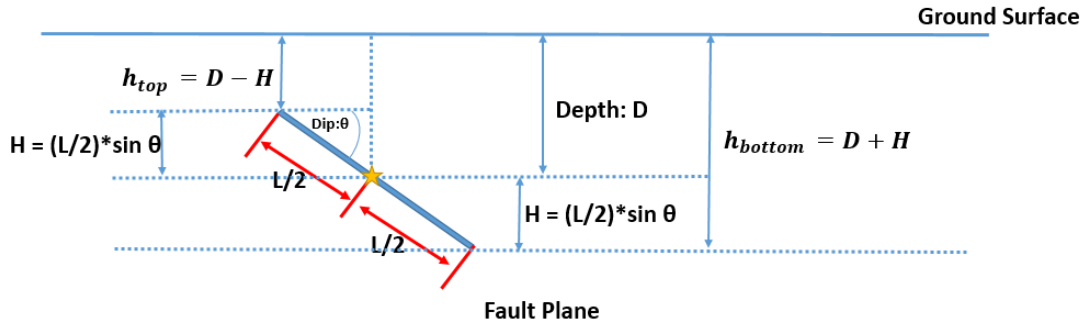

Fig. 19. Schematic illustration of fault top depth and fault bottom depth calculations.

For fault top and bottom depth calculations, h-top is the fault top depth, and h-bottom is the fault bottom depth. θ is the dip angle. Thus,

$$h_{top} = D - \left(\frac{L}{2}\right)\sin\theta \cdots\cdots\cdots\cdots\cdots\cdots 3$$

$$h_{bottom} = D + \left(\frac{L}{2}\right)\sin\theta \cdots\cdots\cdots\cdots\cdots\cdots 4$$

Now for the map view fault starting and fault ending points, $(\boldsymbol{X_{Start}}, \boldsymbol{Y_{start}})$ and $(\boldsymbol{X_{end}}, \boldsymbol{Y_{end}})$ correspondingly, the schematics and equations are as follows. Notice that the strike is with respect to the north, the start point and ending point are on the fault top.

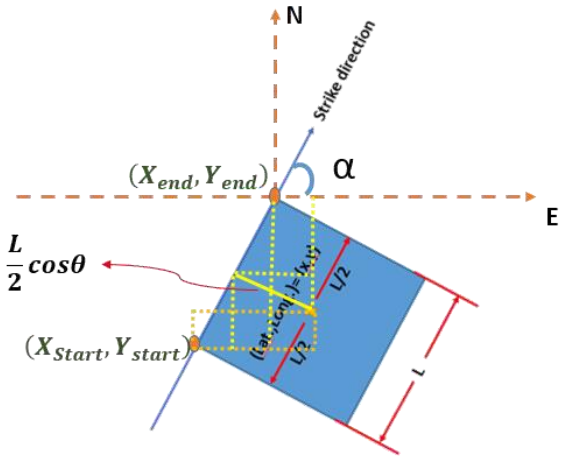

Fig. 20: Illustration of fault top depth and fault bottom depth calculations.

For Coulomb input file format convenience, the starting point and ending point are calculated as equations 5, 6, 7, 8.

(X_{Start}, Y_{start}):

$$X_{Start} = X - \left(\frac{L}{2}sin\alpha - \frac{L}{2}cos\theta cos\alpha\right) \cdots 5$$

$$Y_{start} = Y - \left(\frac{L}{2}cos\theta sin\alpha + \frac{L}{2}cos\alpha\right) \cdots 6$$

(X_{end}, Y_{end}) :

$$X_{end} = X + \left(\frac{L}{2}cos\theta cos\alpha + \frac{L}{2}sin\alpha\right) \cdots 7$$

$$Y_{end} = Y - \left(\frac{L}{2}cos\theta sin\alpha - \frac{L}{2}cos\alpha\right) \cdots 8$$

With the above calculations, I created a full receiver faults input file for the focal-mechanisms data set (Fig. 21).

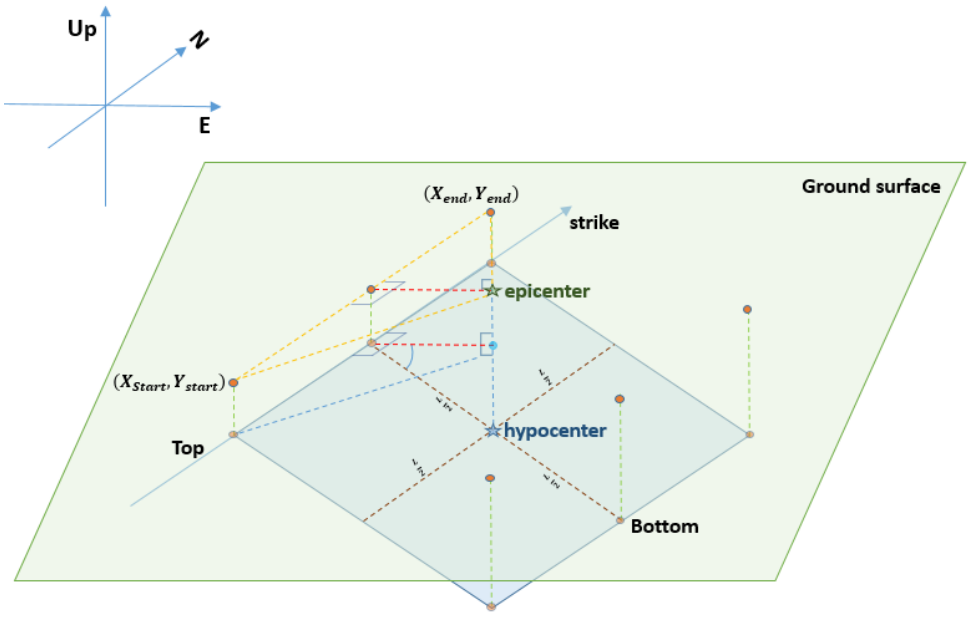

Fig. 21. A 3D view of the model setting up. The green rhombus represents the ground surface; the blue rhombus is the underground fault surfaces calculated based on earthquake magnitude. Hypocenter and epicenter are marked as stars.

The above stress-inversion of FMS in Oklahoma revealed relatively uniform stress state in both time and space (Fig. 11, 13). An efficient way to generate a uniform stress field in Coulomb program is to define a source fault, which is a virtual, large fault that generates a uniform stress state in the area of interest. The rake of the source strike-slip fault plane follows Coulomb's convention, schematics is shown in Fig. 22 (Toda, et al., 2011). Rake is the angle measured in the plane of the fault between the reference strike (right-hand rule) and the slip vector (Cronin, 2010). In order to generate maximum shortening direction of 80° from north clockwise, the source strike-slip fault has a right-lateral motion, thus the rake of which is 180°.

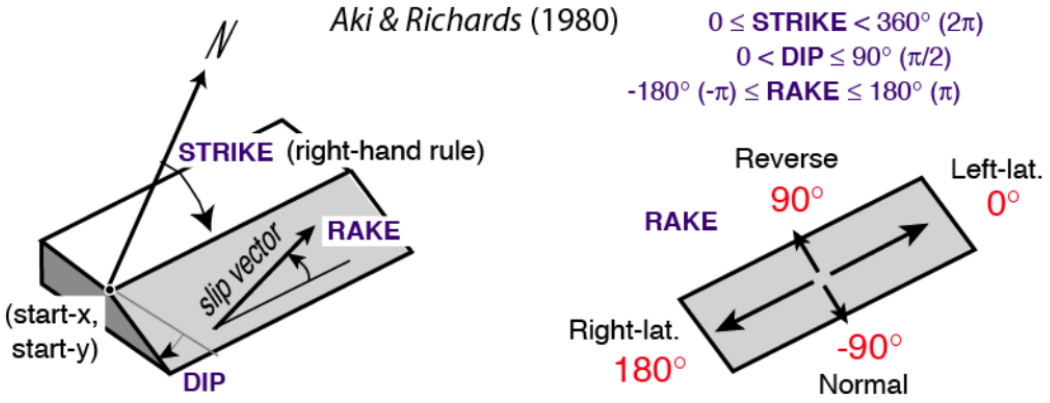

Fig. 22. Convention for resolving stress and for focal-mechanisms (Toda, et al., 2011).

Fig. 23 shows the schematic illustration of source strike-slip fault and the σ_1 directions generated by the source. The source strike-slip fault with a right-lateral motion in the strike of 125° in a purple line. Blue arrows show the maximum compressional stress direction. The strike of the testing point is perpendicular to the maximum shortening direction and it is marked in green line.

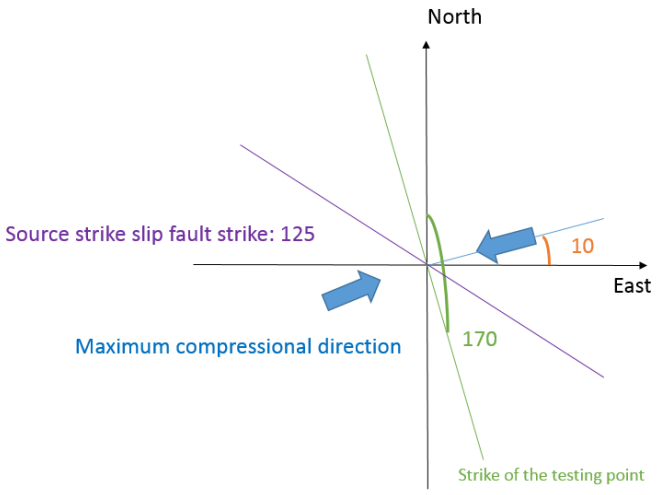

Fig. 23. Schematic illustration of the source strike-slip fault and the maximum compression direction.

After many trial-and-error attempts for a uniform stress field, I selected a source fault that strikes 125°, it is 10,000 km long and 5,000 km deep with net right-lateral strike-slip displacement of 100 m. This strike-slip fault generates a uniform stress field in Oklahoma with □HMAX axis in azimuth 80°. The stress changes due to this source fault were calculated at a point in the area of the FMS (Fig. 24), for seven receiver faults (Table 5). The source fault is plotted at the SW part of the map.

Table. 5. Testing point stress change with different orientations

Testing Point Location			**Receiver Slip (degree)**			**Stress Change (bars)**		
X (km)	**Y (km)**	**Z (km)**	**Strike**	**Slip**	**Rake**	**Shear**	**Normal**	**Coulomb**
100	0	5	0	90	180	1.078	-3.324	0.414
100	0	5	45	90	180	3.278	1.033	3.484
100	0	5	90	90	180	-1.078	3.232	-0.432
100	0	5	135	90	180	-3.278	-1.124	-3.503
100	0	5	160	90	180	-1.281	-3.250	-1.931
100	0	5	**170**	90	180	-0.108	**-3.495**	-0.807
100	0	5	180	90	180	1.078	-3.324	0.414

The map in coordinates are altered by Coulomb3.3, and the latitude and longitude of the point (0,0) in the map is (35.5 N, 98W). With the change of difference source strike-slip fault strikes, the testing point responses with different stress changes. The source strike-slip fault that gives a maximum shortening direction of 80°from north clockwise are determined, and its strike is 125° from north, clockwise.

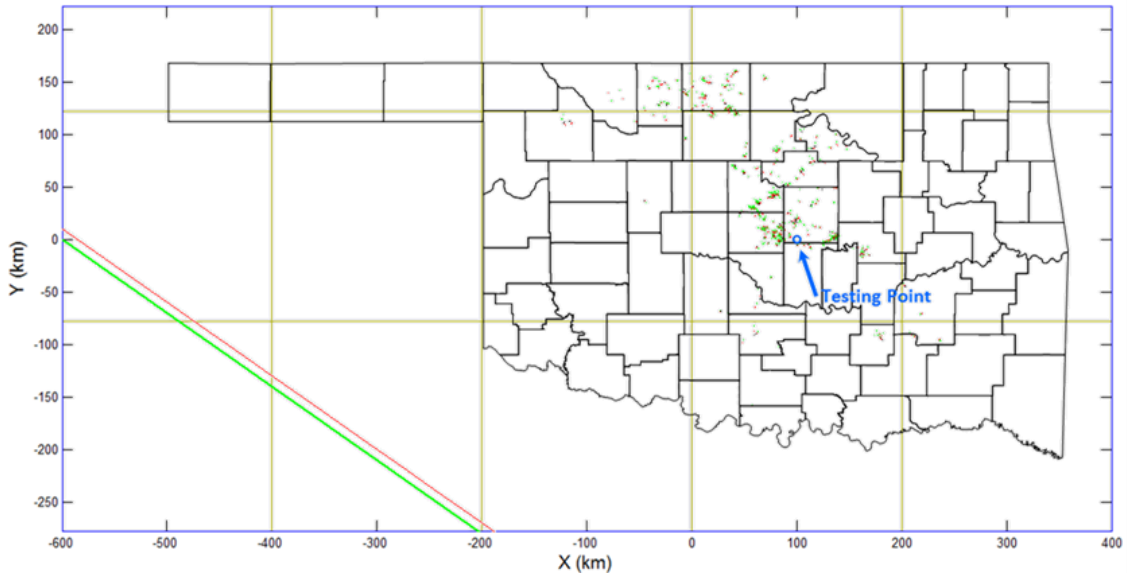

Fig. 24. Testing point location plot in study area at Coulomb3.3 software. The source strike-slip fault is on the bottom left and the testing point is marked in blue circle.

Result of Coulomb3.3 Calculations

Coulomb Stress Change, ΔCFF

I derived above a uniform stress state from the stress-inversion (section 'The stress field in Oklahoma'), and found an effective way to apply this uniform stress on the region of earthquakes in Oklahoma (Fig. 23). Now, I use these results to calculate the change of Coulomb Failure Function, ΔCFF, on the 562 faults for which focal-

mechanism was determined. These faults are regarded as receiver faults, and I calculated ΔCFF for three options: right-lateral slip, reverse slip and normal faulting.

The first calculations is ΔCFF for right-lateral slip (Fig. 25) and zoomed-in view for the Prague earthquake area (Fig. 26). The color bar here, from cold color to warm color, indicates the negative to positive stress change on individual faults. The warmer the color bars, the higher possibility of right-lateral slip, and vice versa. In Fig. 26, of Prague area, the faults that strike NE-SW have increasing possibility for right-lateral slip, showing an orange warm color. Whereas the faults that have NW-SE strikes have high possibility for left-lateral slip, showing with blue toned color. The detailed output results are saved as 'element conditions. csv' which will be used later.

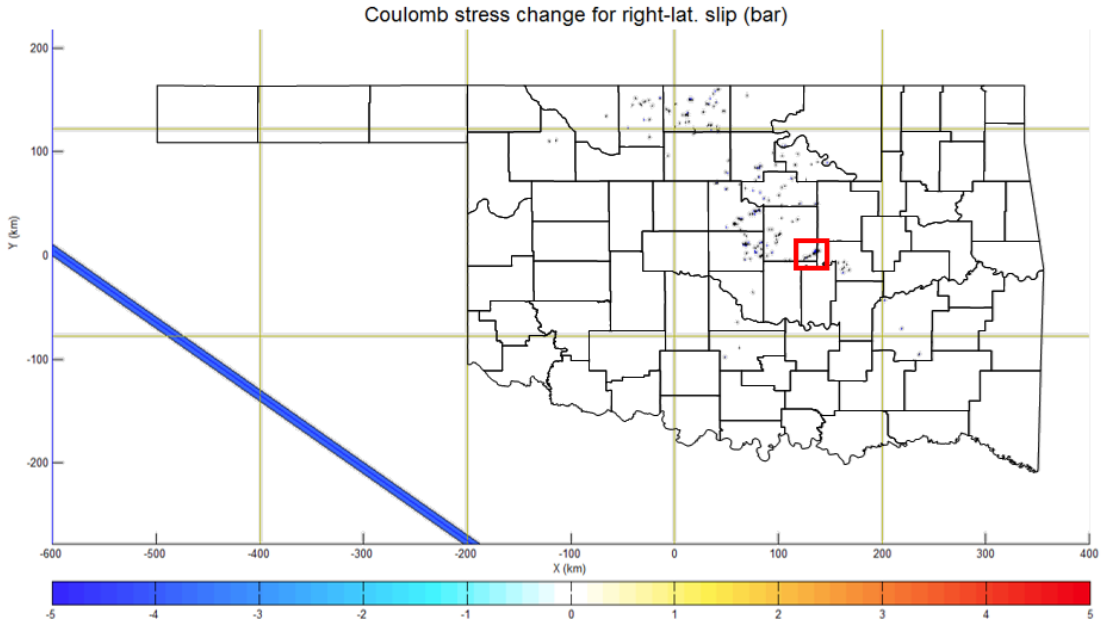

Fig. 25. Coulomb stress change for right-lateral slip on receiver faults. The color bar here, from cold color to warm color, indicates the negative to positive stress change on individual faults. The warmer the color bars, the higher possibility of right-lateral slip, and vice versa. Red box is the zoomed in location of Fig. 26.

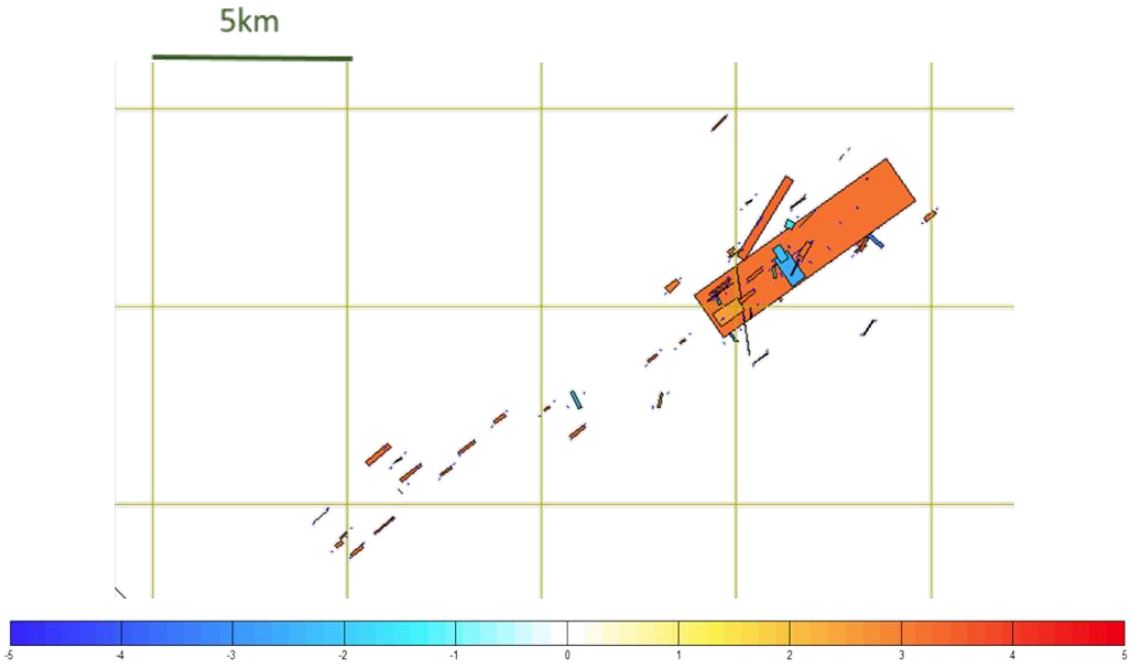

Fig. 26. Zoomed-in view of Coulomb stress change for right-lateral slip at Prague.

The second case includes ΔCFF calculations for reverse slip (Fig. 27) with zoomed-in view of the Prague area (Fig. 28).

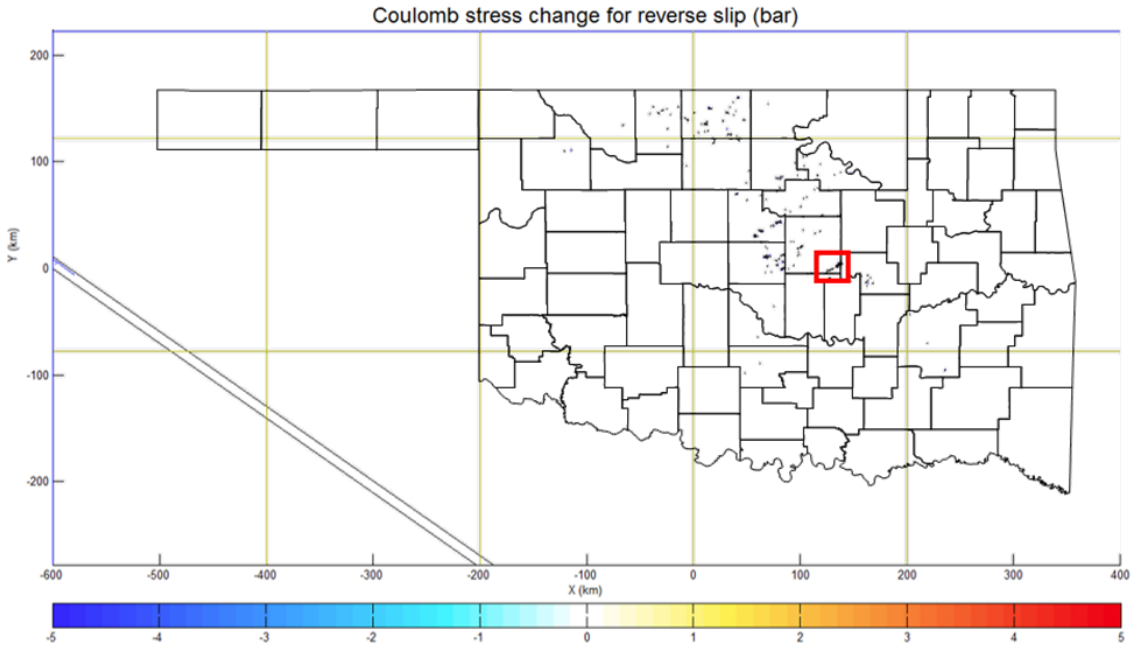

Fig. 27. Coulomb stress change for reverse slip on receiver faults.

In Fig. 28, the faults that strike NE-SW slightly negative to zero ΔCFF, meaning the stress field strike-slip will slightly suppress to reverse slip. Noticeably, the faults that strike NW-SE have positive stress change on reverse slip, appearing in yellow color.

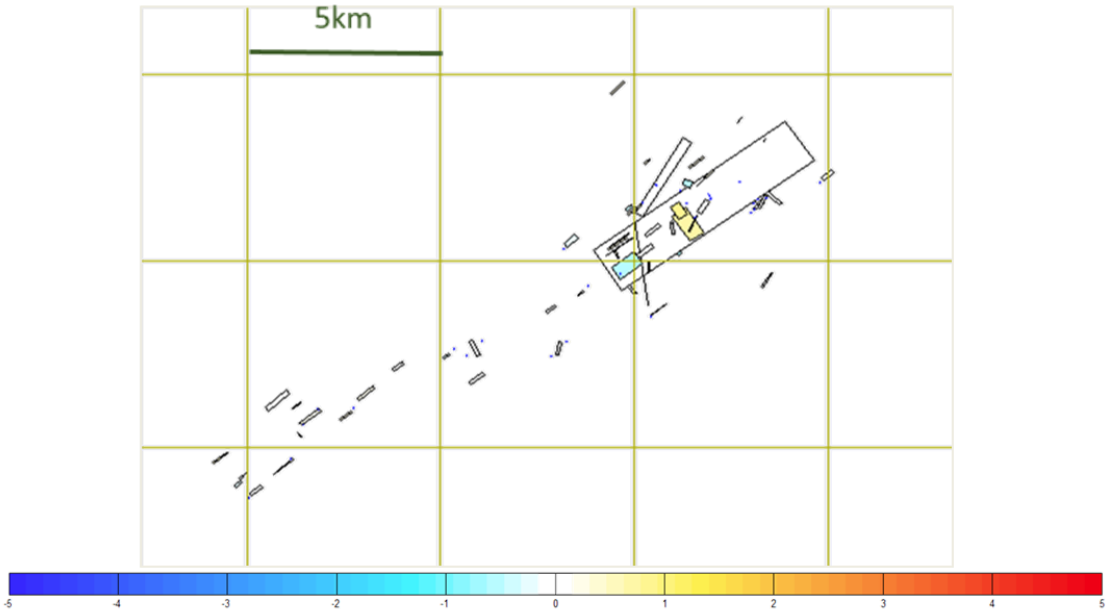

Fig. 28. Zoomed-in view of Coulomb stress change for reverse slip at Prague.

The third part of ΔCFF calculations is the normal stress change on faults. Fig. 29 and 30 are the output map. In the zoomed-in map of Fig. 30, the large NE-SW fault in Prague area has positive ΔCFF, representing that this fault has an increased possibility of clamping under the stress from source strike-slip fault. On the opposite, the NW-SE fault is blue toned, meaning the stress field suppresses this fault to clamp.

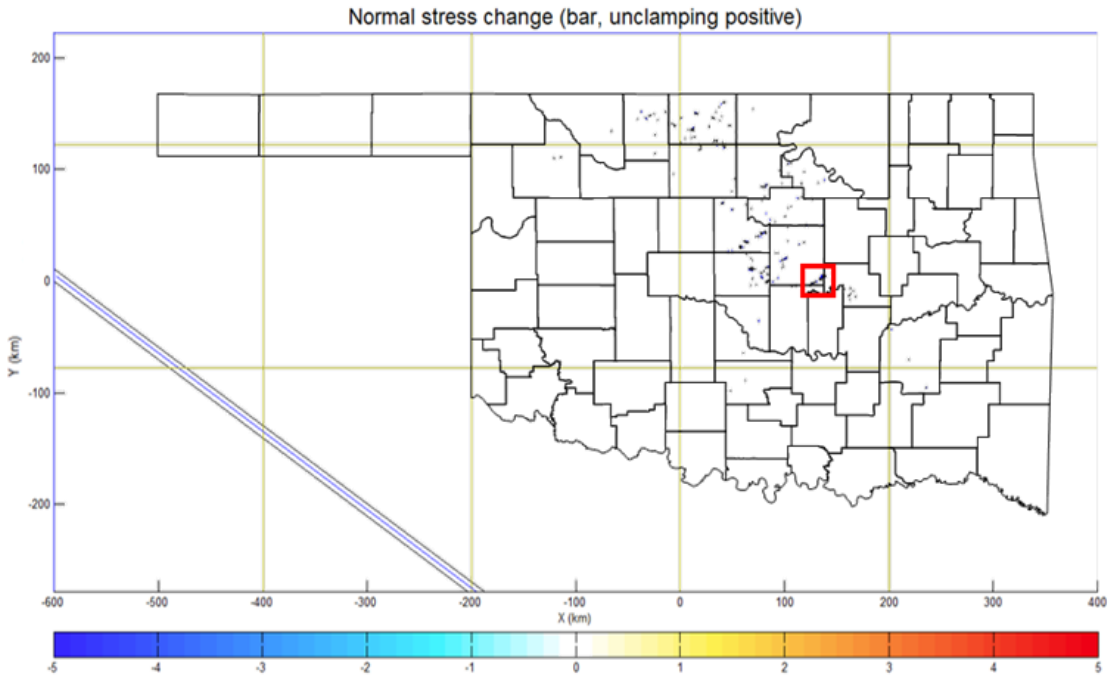

Fig. 29. Normal stress change on receiver faults.

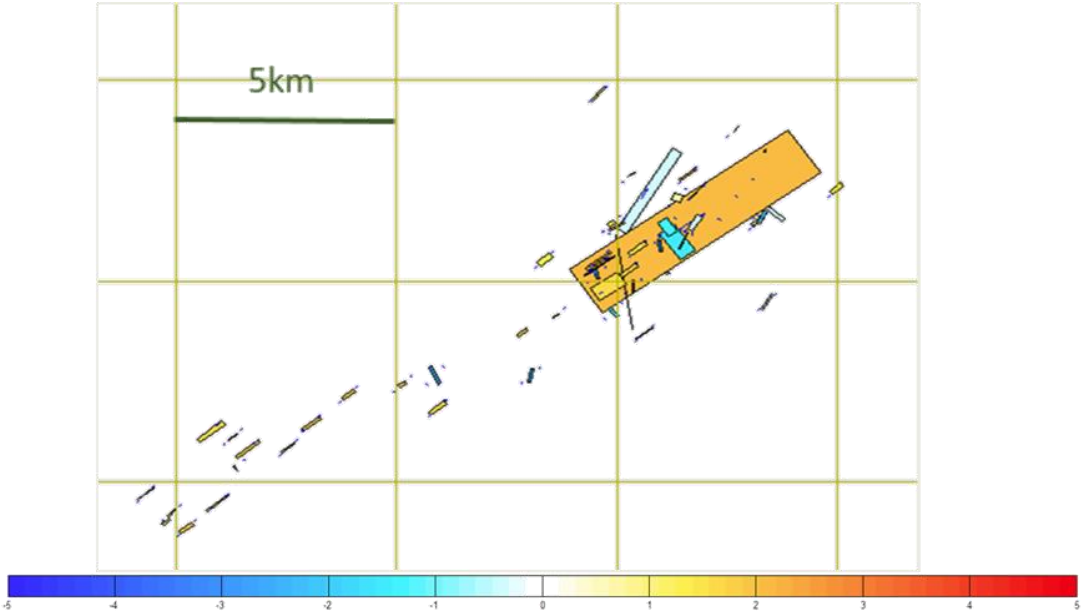

Fig. 30. Zoomed-in view of normal stress change on the faults at Prague area.

Synthesis of Coulomb 3.3 Calculations

The output file 'element condition.csv' provides the info on the change of Coulomb failure function that was presented in Figs. 25-30 above. From this file, I plotted frequency histograms (Fig. 31) of ΔCFF for the three cases: right-lateral slip, reverse slip, and normal slip.

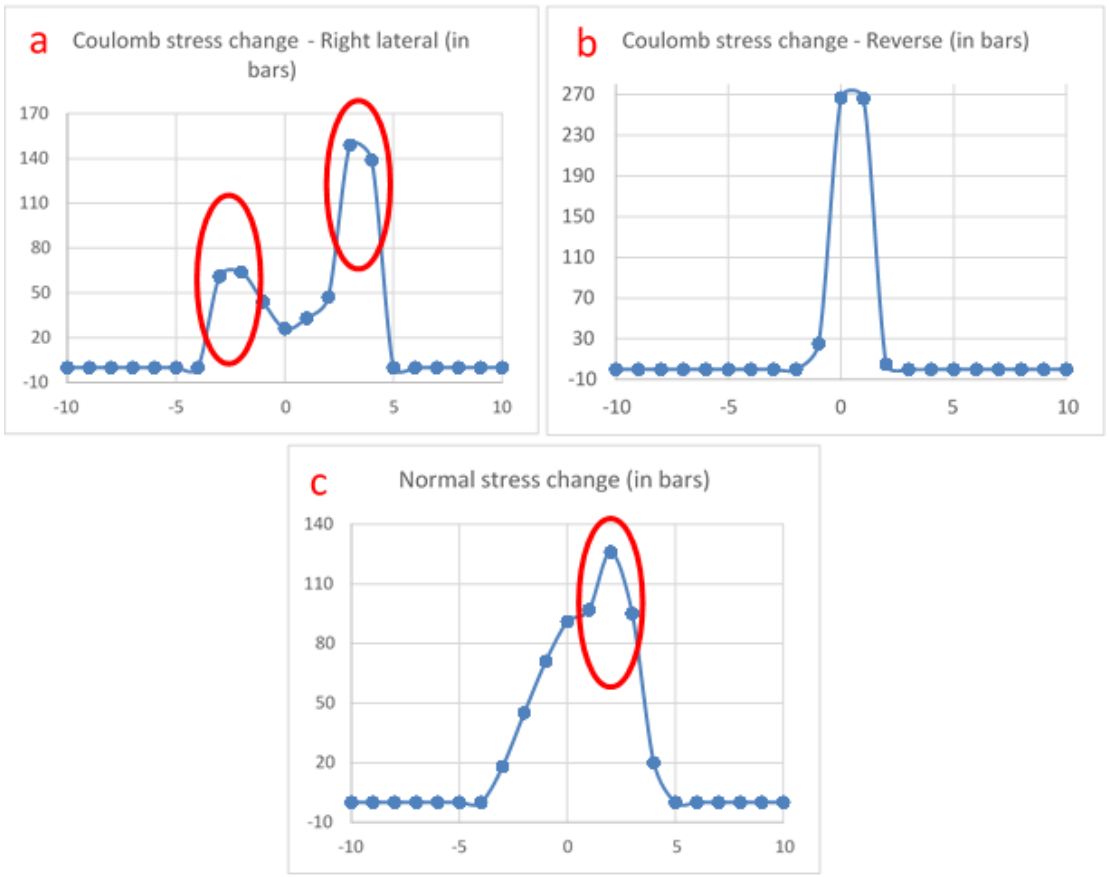

Fig. 31. Coulomb stress change on faults results: a. Histogram of Coulomb stress change on faults of right-lateral slip. b. Histogram of Coulomb stress change of reverse slip on faults. c. Normal stress change on faults histogram. Red circles in Fig. 31a are the peaks of Coulomb stress change on right-lateral slip, and peak of normal stress change in Fig. 31c.

Fig. 31a (right-lateral) displays two peaks that correspond to the two portions in the rose diagram of FMS results in Fig. 16. The NE-SW faults have an increasing possibility for right-lateral slip, and they are shown as the right peak in Fig. 31a. The NW-SE faults are more likely to have left-lateral slip, which are shown as the left peak of Fig. 31a. Fig. 31b (reverse slip) displays one around zero that indicates little tendency of reverse slip. Fig. 31c (normal slip) also shows one peak, but it is wider, $\Delta CFF = -4$ to $\Delta CFF = 5$, indicating favorable conditions for normal faulting on some of the faults. This pattern corresponds to the stress-inversion results (Fig. 11) that some faults have normal motions.

The Red circles marked in Fig. 31 a left peak, right peak and Fig. 31c are those faults that have increasing tendency of left-lateral slip, right-lateral slip and unclamping. The locations of these events are plotted in Fig. 32 a, b, c with faults strike rose diagrams.

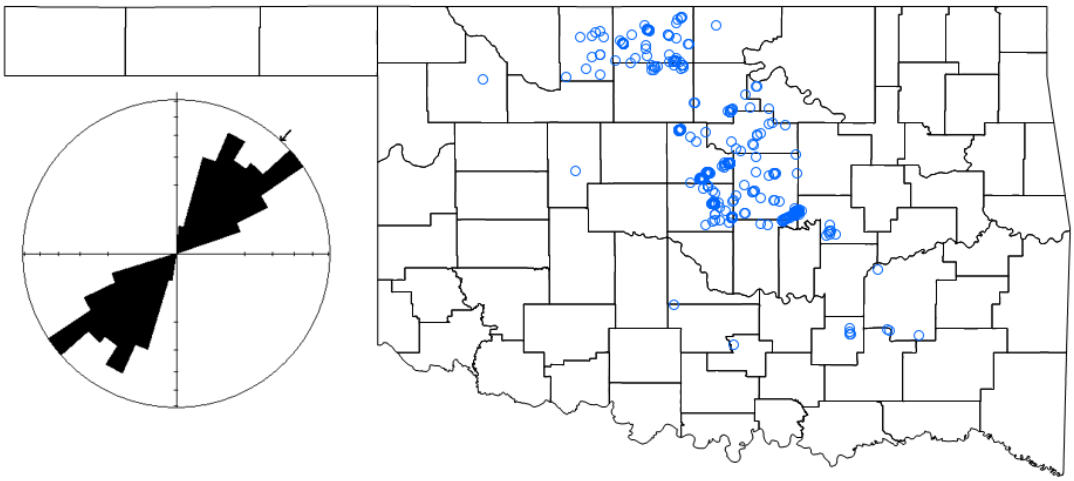

Fig. 32a. Locations of the faults that have increasing possibility of right-lateral slip. Rose diagram of these faults strikes are plotted. Fault locations are marked in blue open circles.

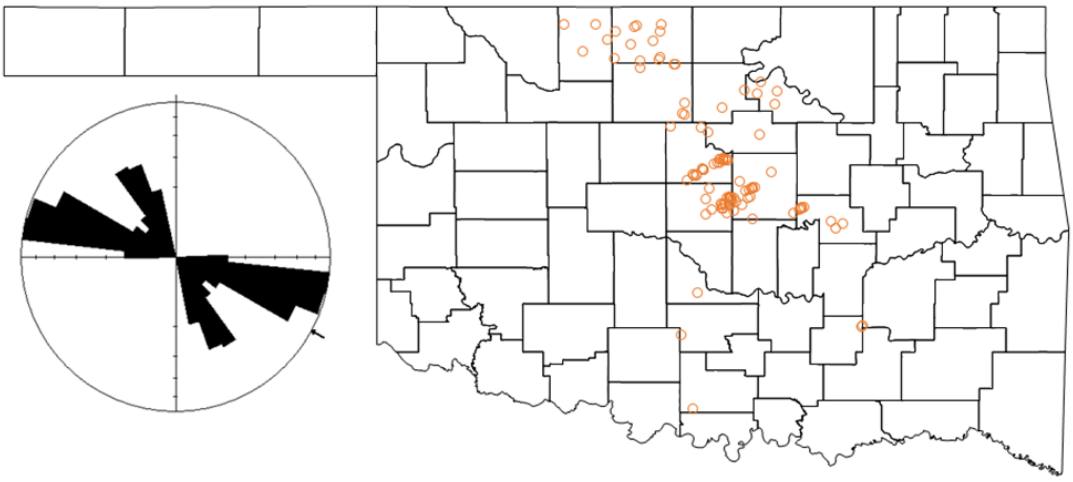

Fig. 32b. Locations of the faults that have increasing possibility of left-lateral slip. Rose diagram of these faults strikes are plotted. Fault locations are marked in orange open circles.

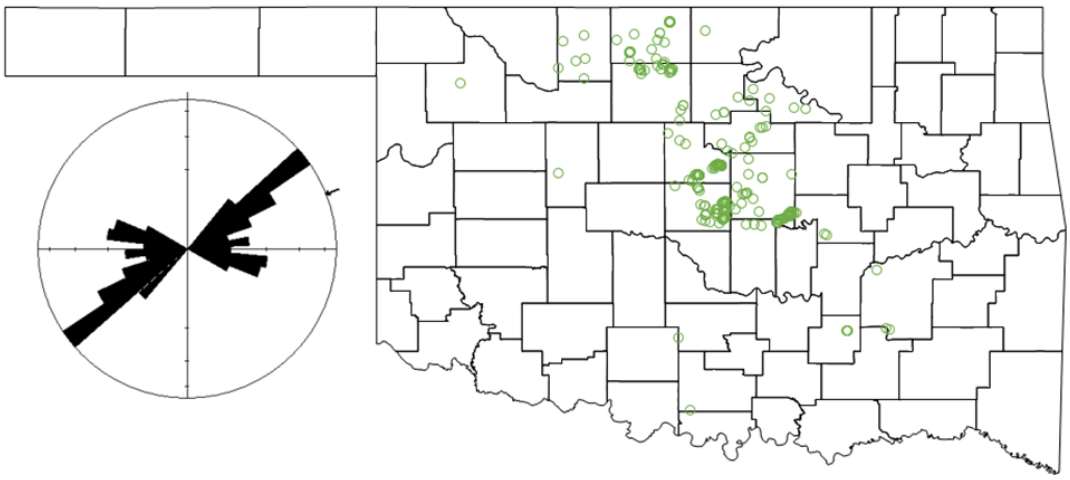

Fig. 32c. Locations of the faults that have increasing possibility of unclamping. Rose diagram of these faults strikes are plotted. Fault locations are marked in green open circles.

Fig. 32 a, b, c indicated that the faults that have increasing possibility of right-lateral slip, left-lateral slip, and unclamping are widely spread, without clear regional

clustering. The rose diagrams of these faults indicate that the faults that have NE−SW have more likely to have right-lateral slip. Faults that have strike 115°, 145° tend to have left-lateral slip, and faults that have 55° and 110° are more likely to unclamp. These results are also shown by zoomed-in area of Prague in Figs. 26, 28, 30.

Summary and Conclusions

The present analysis focuses on the in-situ stress field in Oklahoma. It is based on stress-inversion (Reches, 1987) of focal-mechanism solutions (FMS) from January 2010 to February 2015. The stress-inversion program, Stress, allows the best fit friction coefficient to be calculated, and to separate between the 'real' and 'auxiliary' planes in the double-couple of a focal solution.

The present stress-inversion calculations for Oklahoma FMS indicate:

1. The effective friction coefficient for this dataset is $\mu = 0.2$ (Fig. 9). It should noted that pore-pressure cannot be independently determined in the stress program, and thus, the low friction coefficient may indicate elevated pore-pressure.
2. Most of FMS indicate oblique strike-slip faults and normal components, with two dominant strike directions: NE-SW (40°—220°) and NW-SE (128°—308°) (Fig. 16).
3. The calculated in-situ stresses appears stable over the observation period (five years) and for the entire area of activity (~ 200 x 200 km) (Figs. 6, 7, 11).
4. The maximum horizontal extension is strongly bounded to σ_{hmin} = 350°-360°; most solutions indicate strike-slip relations of $\sigma_{HMAX} > \sigma_{vertical}$; fewer solution indicate transition between strike-slip and normal faulting, namely $\sigma_{HMAX} \sim \sigma_{vertical}$ (Figs. 11, 12).
5. To apply the in-situ stress results to Oklahoma fault system, the fault map was divided into three zones based on the tectonic style (Fig. 13). The recent earthquakes, in general, and the earthquakes with FMS, in particular, are almost

exclusively in Zone B, which is in the north-center part of Oklahoma (Fig. 7). However, the trends of the FMS faults display good agreement with the trends of faults in Zone A, partly in Zone C, and poor agreement with fault trends of zone B (Fig. 16b). Many of the faults in Zones A and C are basement controlled, and thus it appears that the earthquakes occurred along reactivated basement faults (Fig. 16 a, c).

In a reverse process of the stress-inversion, I used the Coulomb3.3 program for forward calculations of the stress conditions on Oklahoma faults. A very long, right-lateral strike-slip fault was used to generate a uniform stress field in Oklahoma (Figs. 23, 24), and all FMS faults were converted to receiver faults with sizes according to the seismic magnitude (Fig. 17). The program calculates the Coulomb stress change parameter, ΔCFF, that indicates the likelihood for slip along the focal-mechanism fault due to the regional stress. The calculations show:

1. An increase of ΔCFF (tendency to slip increase) for right-lateral slip along faults that trend NE-SW, and for left-lateral slip along faults that trend NW-SE (Figs. 25, 26).
2. Majority of faults are not likely to have reverse slip, whereas many of them are likely to slip as normal faults (Figs. 27, 28, 29, 30).
3. These results are consistent with the stress-inversion results, as expected.

References

Aki, K., and P. G. Richards 1980, Quantitative Seismology, Theory and Methods. Volume I: 557 pp., 169 illustrations. Volume II: 373 pp., 116 illustrations. San Francisco: Freeman.

Angelier, J., 1984, Tectonic analysis of fault slip data sets, J. Geophys Res., 89. 5835-5848.

Bott, M . H. P., 1959, The mechanics of oblique slip faulting Geol. Mag., 96, 109-117.

Byerlee, J., 1978, Friction of rocks, Pure and Applied Geophysics, Vol. 116, Issue. 4, pp 615-626

Cronin, V., 2010, A primer on focal mechanism solution for geologists.

Darold, A., and A. Holland, 2015, Preliminary Oklahoma Optimal Fault Orientations, Oklahoma Geological Survey Open File Report, OF4-2015.

Ellsworth, W. L., 2013, Injection-Induced Earthquakes, Science 341, 1225942 (2013). DOI: 10.1126/science.1225942

Gephart, J. W. and Forsyth, D. W., 1984, An improved method for determining the regional stress tensor using earthquake focal mechanism data: Application to the San Fernando Earthquake Sequence, J. Geophys. Res., 89(B11), pp 9305–9320.

Holland, A., 2013, Earthquakes triggered by hydraulic fracturing in south‐central Oklahoma, Bull. Seismol. Soc. Am. 103, 1784‐1792.

Johnson, K. S., 2008, Geologic History of Oklahoma, Educational publication 9, Oklahoma Geological Survey.

Keranen, K. M., Savage, H. M., Abers, G. A., and E. S. Cochran, 2013, Potentially induced earthquakes in Oklahoma, USA: Links between wastewater injection and the 2011 Mw 5.7 earthquake sequence, Geology, doi: 10.1130/G34045.1.

Keranen, K., Weingarten, M., Abers, G., Bekins, B., and Ge, S., 2014, Sharp increase in central Oklahoma seismicity since 2008 induced by massive wastewater injection, Science 345, 448–451.

Lin, J. and R.S. Stein, 2004, Stress triggering in thrust and subduction earthquakes, and stress interaction between the southern San Andreas and nearby thrust and strike-slip faults, Journal of Geophysical Research, v. 109, B02303, doi:10.1029/2003JB002607.

Luza, K. V., 2008, Earthquakes of Oklahoma, Oklahoma Geological Survey, Educational Publication 9, Earthquakes, pp. 9.

McGarr, A., Bekins, B., Burkardt, N., Dewey, J., Earle, P., Ellsworth, W., Ge, S., Hickman, S., Holland, A., Majer, E., Rubinstein, J., and A. Sheehan, 2015, Coping with earthquakes induced by fluid injection. Science, v. 347, p. 830-831. [DOI:10.1126/science.aaa0494]

McNamara, D. E., H. M. Benz, R. B. Herrmann, E. A. Bergman, P. Earle, A. Holland, R. Baldwin, and A. Gassner, 2015, Earthquake Hypocenters and Focal Mechanisms in Central Oklahoma Reveal a Complex System of Reactivated Subsurface Strike-Slip Faulting, AGU Geophysical Research Letter, 10.1002/2014GL062730

Michael, A. J., 1984, Determination of stress form slip data: faults and folds, Journal of Geophysical Research, VOL. 89, NO B13, pp 11,517—11,526.

Michael, A. J., 1987, Use of focal mechanisms to determine stress: A control study, Journal of Geophysical Research, VOL. 92, Issue B1, pp 357—368.

Northcutt and Campbell, 1998, Basement Tectonics 12. Volume 6 of the series Proceedings of the International Conferences on Basement Tectonics pp 29-37

Northcutt, R. A., and J. A. Campbell, 1995, Geological Provinces of Oklahoma, OGS Open-File Report OF5-95, http://www.ogs.ou.edu/geolmapping.php

Oklahoma Geological Survey, 2016, County data

Peterson, M. D., C. S. Mueller, M. P. Moschetti, S. M. Hoover, A. L. Llenos, W. L. Ellsworth, A. J. Michael, J. L. Rubinstein, A. F. McGarr, and K. S. Rukstales, 2016, 2016 One-Year Seismic Hazard Forecast for the Central and Eastern United States from Induced and Natural Earthquakes, USGS Open-File Report 2016–1035.

Reches, Z., 1987, Determination of the tectonic stress tensor from slip along faults that obey the Coulomb yield criterion, Tectonics, 6,849 -861.

Reches, Z., 1990, The stress states associated with slip along clusters of faults: Application to the aftershocks of Morgan Hill earthquake, 1984 and Kalmata earthquake, 1986.

Reches, Z., 1992, Constraints on the strength of the upper crust from stress inversion of fault slip data, Journal of Geophysical Research, Vol. 97, NO. B9, 12,481- 493.

Shearer, P.M., 1999, Introduction to seismology: Cambridge, Cambridge University Press, 260 p.

Sipkin, S.A., 1982, Estimation of earthquake source parameters by the inversion of waveform data: Synthetic waveforms: Physics of Earth and Planetary Interiors, v. 30, p. 242–259.

Sipkin, S.A., 1986, Interpretation of non-double-couple earthquake mechanisms derived from moment tensor inversion: Journal of Geophysical Research, v. 91, p. 531–547.

Sipkin, S.A., 1994, Rapid determination of global moment-tensor solutions: Geophysical Research Letters, v. 21, p. 1667–1670.

Stover, C. W., B. G. Reagor, and S. T. Algermissen, Seismicity map of the state of New Mexico, U.S. Geol. Surv. Map, MF-1660, 1983.

Toda, S., R. S. Stein, K. Richards-Dinger and S. Bozkurt, 2005, Forecasting the evolution of seismicity in southern California: Animations built on earthquake stress transfer, Journal of Geophysical Research, v. 110, B05S16, doi: 10.1029/2004JB003415.

Toda, S., Stein, R.S., Sevilgen, V., and J. Lin, 2011, Coulomb 3.3 Graphic-rich deformation and stress-change software for earthquake, tectonic, and volcano research and teaching—user guide: U.S. Geological Survey Open-File Report 2011-1060, 63 p., available at http://pubs.usgs.gov/of/2011/1060/.

USArray website, http://www.earthscope.org/science/observatories/usarray

USGS earthquake catalog, http://.earthquake.usgs.gov.

USGS Focal Mechanism website: http://earthquake.usgs.gov/learn/topics/beachball.php

USArray website, http://www.earthscope.org/science/observatories/usarray

Walsh III, F. R., and Zoback, M. D., 2015, Oklahoma's recent earthquakes and saltwater disposal, Science Advances, Vol. 1, no. 5, e1500195, DOI: 10.1126/sciadv.1500195

Wells, D. L. and K. J. Coppersmith, 1994, New Empirical Relationships among Magnitude, Rupture Length, Rupture Width, Rupture Area, and Surface Displacement, Bullentin of the Seismological Society of America, Vol. 84, No. 4, p. 974-1002.